

Article

# A Cluster-Type Self-Healing Catalyst for Stable Saline–Alkali Water Splitting

Haiming Wang<sup>1,2</sup> and Sheng Chen<sup>1,\*</sup> 

<sup>1</sup> Key Laboratory for Soft Chemistry and Functional Materials (Ministry of Education), School of Chemical Engineering, Nanjing University of Science and Technology, Nanjing 210094, China

<sup>2</sup> College of Mechanical and Electronic Engineering, Tarim University, Alaer 843300, China

\* Correspondence: sheng.chen@njust.edu.cn

**Abstract:** In electrocatalytic processes, traditional powder/film electrodes inevitably suffer from damage or deactivation, reducing their catalytic performance and stability. In contrast, self-healing electrocatalysts, through special structural design or composition methods, can automatically repair at the damaged sites, restoring their electrocatalytic activity. Here, guided by Pourbaix diagrams, foam metal was activated by a simple cyclic voltammetry method to synthesize metal clusters dispersion solution (MC/KOH). The metal clusters-modified hydroxylated Ni-Fe oxyhydroxide electrode (MC/Ni<sub>x</sub>Fe<sub>y</sub>OOH) by a facile Ni-Fe metal–organic framework-reconstructed strategy, exhibiting superior performance toward the oxygen evolution reaction (OER) in the mixture of MC/KOH and saline–alkali water (MC/KOH+SAW). Specifically, using a nickel clusters-modified hydroxylated Ni-Fe oxyhydroxide electrode (NC/Ni<sub>x</sub>Fe<sub>y</sub>OOH) for OER, the NC/Ni<sub>x</sub>Fe<sub>y</sub>OOH catalyst has an ultra-low overpotential of 149 mV@10 mA cm<sup>−2</sup>, and durable stability of 100 h at 500 mA cm<sup>−2</sup>. By coupling this OER catalyst with an efficient hydrogen evolution reaction catalyst, high activity and durability in overall SAW splitting is exhibited. What is more, benefiting from the excellent fluidity, flexibility, and enhanced catalytic activity effect of the liquid NC, we demonstrate a self-healing electrocatalysis system for OER operated in the flowing NC/(KOH+SAW). This strategy provides innovative solutions for the fields of sustainable energy and environmental protection.

**Keywords:** nickel clusters; saline–alkali water; oxygen evolution reaction; self-healing; activity; stability



**Citation:** Wang, H.; Chen, S. A Cluster-Type Self-Healing Catalyst for Stable Saline–Alkali Water Splitting. *Catalysts* **2024**, *14*, 81. <https://doi.org/10.3390/catal14010081>

Academic Editor: Bruno Fabre

Received: 27 December 2023

Revised: 10 January 2024

Accepted: 16 January 2024

Published: 18 January 2024



**Copyright:** © 2024 by the authors. Licensee MDPI, Basel, Switzerland. This article is an open access article distributed under the terms and conditions of the Creative Commons Attribution (CC BY) license (<https://creativecommons.org/licenses/by/4.0/>).

## 1. Introduction

Water electrolysis refers to the process of splitting water into hydrogen and oxygen gases through electrolysis. It provides a viable method for storing electrical energy and creating clean hydrogen fuel that could offer new solutions for combating climate change and achieving carbon neutrality. However, the slow kinetics of the oxygen evolution reaction (OER) half-reaction in water splitting results in high energy consumption [1–3]. In order to address this issue, highly active noble metal catalysts (i.e., RuO<sub>2</sub> and IrO<sub>2</sub>) are selected in water splitting, but their high price and scarcity significantly increase the cost of the catalyst [1,2,4]. However, most of those catalysts require freshwater or low-grade water via pre-treatment using external purification/desalination plants as an electrolyte; this exacerbates the consumption of scarce freshwater resources and the associated investment costs [5,6].

In contrast, there is a widespread distribution of abundant low-quality water on earth, such as seawater and inland saline–alkali water (SAW). If the synthesized electrodes can be directly used or subjected to simple treatment for electrolytic hydrogen production from low-quality water, it would be crucial for achieving sustainable utilization of clean energy and environmental protection [6]. However, compared to pure water splitting, the use of seawater for electrolysis presents additional challenges for the required catalysts due to the corrosive nature of chloride ions, the poisonous effect of impurities, and the deposition

of precipitates present in seawater [4,6,7]. For this purpose, researchers have conducted studies focusing on seawater and have proposed several common guiding principles [8–11]. However, there is still controversy regarding the application of these methods to other types of low-quality water. Further development of electrodes with high activity, durability, and cost-effectiveness is needed to carry out in-depth research on hydrogen production from other low-quality water sources and promote their high value-added utilization.

In electrocatalytic processes, traditional powder/film electrodes inevitably suffer from damage or deactivation (i.e., dissolution, corrosion, protonation), reducing their catalytic performance and stability. In contrast, self-healing electrocatalysts, through special structural design or composition methods, can automatically repair at the damaged sites, restoring their electrocatalytic activity. Recently, self-healing electrocatalysts have become a new class of functional materials. Nocera's team drew inspiration from photosynthesis in plants in situ to form oxygen-evolving catalysts with good photocatalytic activity in neutral water containing phosphate and  $\text{Co}^{2+}$ . This has sparked a research trend in self-healing catalysts [12]. Furthermore, Nocera's team focused on synthetic cobalt phosphate catalysts and explored the repair mechanism of self-healing catalysts at the microscopic level. They provided a quantitative model for self-healing and deepened our understanding of the healing mechanism of self-healing catalysts [13]. Recently, Nocera provided a comprehensive review of common self-healing OER catalysts. They offered a clear definition of self-healing and conducted a summary analysis of transition metal-based (nickel, iron, cobalt, manganese, copper, etc.) self-healing catalysts for the OER [14]. Other researchers have also made significant contributions to the study of self-healing catalysts. Li's group proposed the use of Co as a catalyst for the oxidation and redeposition of iron hydroxide to improve the efficiency of Fe redeposition under OER operating potentials. Based on this concept, they proposed a co-catalytic self-healing mechanism and designed a borate-intercalated NiCoFe-LDH catalyst. Through experiments, they determined that this catalyst exhibited excellent self-healing ability under alkaline conditions, while maintaining high activity [15]. The concept of dynamically stable active sites has been proposed by Markovic. By controlling the dissolution and redeposition of the active component iron, a dynamic equilibrium state is maintained, thereby extending the catalyst's lifespan [16]. Wu's research group has developed a method for preparing bismuth nano-catalysts controlled by electrochemical kinetics in liquid metal Ga. When the bismuth catalyst becomes deactivated due to prolonged operation, the self-healing process of the catalyst after deactivation is achieved through in situ electrochemical reconstruction [17]. Currently, common self-healing catalytic electrodes are mainly based on metal ions such as  $\text{Fe}^{2+}/\text{Ni}^{2+}/\text{Co}^{2+}$  and buffer solutions composed of phosphate, carbonate, or borate [12–15]; however, these have certain limitations in system design. Therefore, it is crucial to design self-healing catalysts that are environmentally friendly and capable of directly or easily treating low-grade water. Similar to seawater, SAW is a low-grade surface saline water, and is widely distributed in the arid and semi-arid regions of northwest China (Table S1). To accommodate crop growth, large areas of saline-alkali soil require significant amounts of freshwater for leaching and salt removal. The leachates (SAW) permeate into drainage channels and eventually flow into rivers. Prolonged discharge of SAW can lead to ecological damage to river ecosystems and a wasteful use of water resources [18].

In this work, guided by Pourbaix diagrams, foam nickel was activated by a simple cyclic voltammetry (CV) to synthesize liquid nickel clusters (NC). The self-supported NC/ $\text{Ni}_x\text{Fe}_y\text{OOH}$  electrode by a facile Ni-Fe metal-organic framework-derived strategy exhibits an ultra-low overpotential and durable stability at industrial current density. By coupling this OER catalyst with an efficient hydrogen evolution reaction catalyst, it exhibits high activity and durability in overall SAW splitting. Most importantly—benefiting from the excellent fluidity, flexibility, and enhanced catalytic activity effect of the liquid NC—we demonstrate a self-healing electrocatalysis system for OER operated in the flowing NC/(KOH+SAW). This would play a positive role in the efficient utilization of low-grade surface water.

## 2. Results and Discussion

### 2.1. Poor Electrocatalytic Performance of $Ni_xFe_yOOH$ in Saline-Alkali Water (SAW)

Hydroxylated nickel-iron electrocatalyst ( $Ni_xFe_yOOH$ ) can promote electron/ion transport and reduce the reaction activation energy. These characteristics make the catalyst highly promising for applications in alkaline water electrolysis. Extensive research and development efforts are being conducted to enhance the efficiency and performance of water electrolysis reactions using this catalyst [1,3,19]. However, there is a lack of research studies on the water splitting of hydroxylated nickel-iron catalyst in low-quality SAW. Further development of electrodes with high activity, durability, and cost-effectiveness is needed to carry out in-depth research on hydrogen production from low-quality water sources and promote their high value-added utilization. To ensure the successful synthesis of  $Ni_xFe_yOOH$  catalyst, a series of structural characterizations have been completed. Firstly, NiFe-MOF was synthesized and used as a precursor for OER reaction. According to XRD analyses (Figure S1a–c), NiFe-MOF shows a well-defined MOF crystal structure as well as strong substrate (NF) peaks at around  $44.73^\circ$ ,  $52.09^\circ$ , and  $76.64^\circ$ . The strongest diffraction peak at  $6.48^\circ$  is ascribed to (020) plane of NiFe-MOF. The formation of NiFe-MOF can be further confirmed by infrared and Raman characterization. In the Raman spectrum (Figure S1d), the peak at  $554\text{ cm}^{-1}$  corresponds to the characteristic band of M-O ( $Ni^{2+}/Fe^{3+}$ ) [19]. The C-H stretching pattern of thiophene ring appears at  $667$  and  $801\text{ cm}^{-1}$  [20]. The peak at  $1085\text{ cm}^{-1}$  is the C=C pattern of thiophene ring [19]. The C-C band appeared at  $1432\text{ cm}^{-1}$ , ascribed to the vibrations of thiophene linkers [20]. It also can be seen that the three peaks at  $1532$ ,  $1340$ , and  $1241\text{ cm}^{-1}$  are attributed to the carboxylic acid group of thiophene [19–22]. Fourier transform infrared (FTIR) spectra (Figure S1e) were also obtained to analyze the surface functional groups. Notably, the characteristic FTIR band of the acidic carbonyl group (C=O) at  $1662\text{ cm}^{-1}$  and tensile vibration of the non-ionized carboxyl group (C-OH) at  $1278\text{ cm}^{-1}$  have disappeared, indicating that the organic ligand is completely deprotonated by coordinating with metal ion [23–27]. After 200 segments of CV activation, the characteristic peaks of NiFe-MOF disappear and show an amorphous structure in the XRD spectra (Figure S1b,c). The Raman spectra (Figure S1d) show that characteristic peaks of NiFe-MOF also disappear, yet, the characteristic peaks of NiOOH appear at  $475$  and  $554\text{ cm}^{-1}$  [28,29]. Further FTIR characterizations (Figure S1e) show that the characteristic peaks of  $1584$ ,  $1521$ , and  $775\text{ cm}^{-1}$  have disappeared; the characteristic peak around  $1372\text{ cm}^{-1}$  has become weaker; and the characteristic peak around  $3640\text{ cm}^{-1}$  has become stronger. This suggests that most NiFe-MOF lose their ligands and reconstitute to  $Ni_xFe_yOOH$ .

Next, the morphology of NiFe-MOF and  $Ni_xFe_yOOH$  was observed by SEM. The results show that the NiFe-MOF honeycomb can be clearly observed. Further observation reveals that the NiFe-MOF honeycomb consists of many disordered NiFe-MOF ribbons (Figure S2a–c). After rapid CV activation of NiFe-MOF,  $Ni_xFe_yOOH$  almost completely inherits the honeycomb structure of the NiFe-MOF (Figure S1f). The SEM element mappings of both NiFe-MOF and  $Ni_xFe_yOOH$  reveal a homogeneous distribution of C, O, S, Ni, and Fe elements throughout the honeycomb (Figure S3a,b). However, there are significant differences in the content of these elements between NiFe-MOF and  $Ni_xFe_yOOH$ . Compared with NiFe-MOF, the content of C and S in  $Ni_xFe_yOOH$  is significantly reduced. Additionally, the C content (20 At%) in  $Ni_xFe_yOOH$  is lower than the O content (52.2 At%) (Figure S4a,b). This result indicates that NiFe-MOF loses some of its organic ligands and undergoes transformation into  $Ni_xFe_yOOH$  after CV activation. The accurate observation by HRTEM (Figure S1g) reveals a lattice spacing of  $0.21\text{ nm}$  corresponding to the (210) plane of NiOOH [30]. This finding is consistent with the results obtained from Raman spectroscopy and energy-dispersive X-ray spectroscopy (EDS). Finally, the OER performances of  $Ni_xFe_yOOH$  catalyst in 1 M KOH and SAW have been studied, respectively. To eliminate the possible contributions of oxidation current densities of  $Ni^{2+}/Ni^{3+\delta}$ , all linear sweep voltammetry curves (LSVs) were recorded by sweeping from high to low potentials (reverse sweep) at the scan rate of  $5\text{ mV s}^{-1}$ . This can determine the overpotentials at small

current densities accurately [31].  $\text{Ni}_x\text{Fe}_y\text{OOH}$  shows a higher overpotential in SAW than in 1 M KOH electrolyte (Figures 1a and S5a,b). Chronopotentiometry measurement is a common method to evaluate the stability of catalysts.  $\text{Ni}_x\text{Fe}_y\text{OOH}$  catalyst in 1 M KOH electrolyte shows good stability but a higher potential (2.8 V (vs. RHE) @500  $\text{mA cm}^{-2}$ , Figure 1b). Compared with 1 M KOH electrolyte, the SAW contains a large amount of chloride ions and calcium–magnesium ions, which can lead to anode (OER) corrosion and cathode (HER) blockage (Table S1a,b) [6],  $\text{Ni}_x\text{Fe}_y\text{OOH}$  catalyst becomes unstable in SAW for a short time (Figure 1b). The results show that the  $\text{Ni}_x\text{Fe}_y\text{OOH}$  catalyst exhibited poor performance in the low-grade SAW. Given this, some measures urgently need to be taken to solve this bad situation. Self-healing electrocatalysts, through special structural design or composition methods, can automatically repair at the damaged sites, restoring their electrocatalytic activity. The self-healing catalysts are expected to be a new approach to solve the above-mentioned challenges.

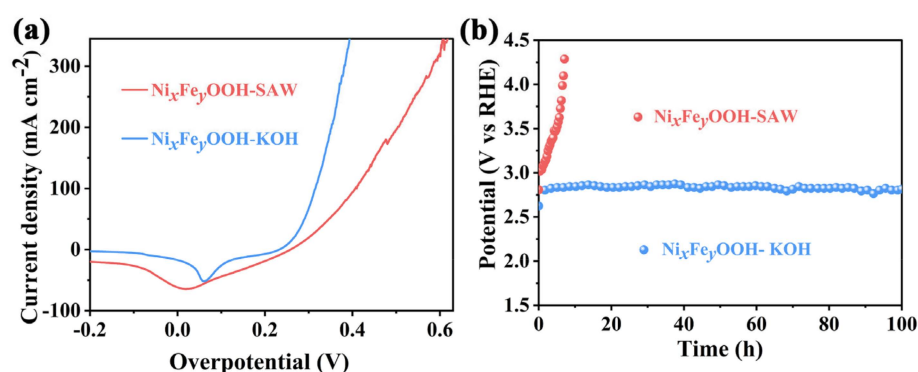


**Figure 1.** (a) OER LSVs of  $\text{Ni}_x\text{Fe}_y\text{OOH}$ ; (b) chronopotentiometry curves of  $\text{Ni}_x\text{Fe}_y\text{OOH}$  at 500  $\text{mA cm}^{-2}$  without iR-compensation which operated in 1 M KOH and SAW, respectively.

## 2.2. Structure Characterization of NC/ $\text{Ni}_x\text{Fe}_y\text{OOH}$ Catalyst

A three-step method for preparing NC/ $\text{Ni}_x\text{Fe}_y\text{OOH}$  catalyst was established, as shown in Figure 2a. A NiFe-MOF self-growing electrode (nickel foam substrate, NF) was firstly prepared by a self-assembly process. This started with the coordination of a highly concentrated precursor solution composed of metal salts (Fe, Ni) and thiophene ( $2\text{-C}_5\text{H}_4\text{O}_2\text{S}$ ). Next, KOH electrolyte with uniform NC was synthesized by activating NF electrode with CV under the guidance of a Pourbaix diagram (E-pH, Figure 2b). This created favorable conditions for subsequent electrode synthesis. Finally, the NiFe-MOF was reconstructed with a similar CV, and it was found that the NiFe-MOF lost its ligand and reconstructed into NC/ $\text{Ni}_x\text{Fe}_y\text{OOH}$  in NC/KOH solution. After the above three steps, the NC/ $\text{Ni}_x\text{Fe}_y\text{OOH}$  catalyst was successfully synthesized and used for OER in SAW. The synthesis of  $\text{Ni}_x\text{Fe}_y\text{OOH}$  is similar to that of NC/ $\text{Ni}_x\text{Fe}_y\text{OOH}$ ; the difference lies in the use of just a KOH electrolyte instead of an NC/KOH mixed electrolyte in the CV activation process of NiFe-MOF. Pourbaix diagrams, also known as E-pH diagrams, provide important information about the stability regions of different chemical species in an electrochemical system. The rational use of Pourbaix diagrams is indeed valuable for the design, synthesis, and selection of electrocatalytic materials [32]. Using Pourbaix phase diagrams of the Ni-water system to guide the synthesis of NC uniformly dispersed in the solution can be a useful approach to enhance the catalytic activity of  $\text{Ni}_x\text{Fe}_y\text{OOH}$ . The NC dispersed in 1–6 M KOH electrolyte have indeed been synthesized by CV activation at a potential range of 1.8 to 2.0 V (vs. RHE) using NF as the working electrode (Figure 2b, see Section 3 for details). It is important to note that specific experimental parameters such as electrolyte concentration, CV activation potential, and cycle numbers may also play a key role in controlling the synthesis and properties of the NC. Careful optimization of these parameters is necessary to achieve the desired characteristics of the synthesized NC. According to Figures S7–S9, the optimum synthesis conditions of NC are as follows: 4 M

KOH electrolyte, 1.8~2.0 V (vs. RHE), 100 cycles of CV. To further verify the universality of the cluster prepared by the CV activated metal foam method, using foamed iron and foamed nickel iron as working electrodes, a similar method was used to synthesize iron clusters (Fe), nickel iron cluster ( $\text{Ni}_{0.5}\text{Fe}_{0.5}$ ) dispersion, nickel iron cluster hydroxyl oxide electrode, and nickel iron cluster hydroxyl oxide electrode. Then, clusters of different metallic element (MC:NC, Fe,  $\text{Ni}_{0.5}\text{Fe}_{0.5}$ ) dispersions were used to OER. As shown in Figure S9c, compared with MC/ $\text{Ni}_x\text{Fe}_y\text{OOH}$  operated in MC/(4 M KOH+SAW) electrolyte, the introduction of NC, Fe, and  $\text{Ni}_{0.5}\text{Fe}_{0.5}$  improves the activity of the MC/ $\text{Ni}_x\text{Fe}_y\text{OOH}$  catalysts operated in the MC/(4 M KOH+SAW) electrolyte, respectively. Further analysis shows that the enhancement activity effect of different kinds of clusters is significantly different. Among them, the contribution of NC is much higher than that of other clusters (Fe clusters,  $\text{Ni}_{0.5}\text{Fe}_{0.5}$  clusters). According to previous reports [3,8,15,22,33,34], the impurity iron in KOH electrolyte may significantly impact the catalytic activity of catalysts. In this work, it is crucial to design a set of experiments aimed at eliminating or weakening the influence of impurity iron in KOH before synthesizing the NC. In order to distinguish between impurity iron in the KOH electrolyte and lattice iron in the NC/ $\text{Ni}_x\text{Fe}_y\text{OOH}$  or  $\text{Ni}_x\text{Fe}_y\text{OOH}$  electrode, we define the impurity iron in the KOH electrolyte as iron ions and the iron in the NC/ $\text{Ni}_x\text{Fe}_y\text{OOH}$  or  $\text{Ni}_x\text{Fe}_y\text{OOH}$  electrode as lattice iron. Based on this distinction, we have extensively discussed the impact of iron ions and lattice iron on different electrodes in Figures 2c and S6. Firstly, by comparing the linear sweep voltammetry (LSV) curves of three different electrodes: NiOOH-KOH (iron ions), NC/NiOOH-KOH (iron ions), and NC/NiOOH-KOH-pure (iron ions free), it can be observed that the LSVs of NC/NiOOH-KOH (iron ions) and NC/NiOOH-KOH-pure (iron ions free) are essentially overlapping. At the same time, significant differences exist when compared to the LSVs of NiOOH-KOH (iron ions). This suggests that the impact of iron ions is negligible, whereas NC plays a pronounced role in enhancing the activity of the NC/NiOOH electrode. Furthermore, by comparing the linear sweep voltammetry (LSV) of three different electrodes:  $\text{Ni}_x\text{Fe}_y\text{OOH}$ -KOH (iron ions), NC/ $\text{Ni}_x\text{Fe}_y\text{OOH}$ -KOH (iron ions), and NC/ $\text{Ni}_x\text{Fe}_y\text{OOH}$ -KOH-pure (iron ions free), it can be observed that the activity of NC/ $\text{Ni}_x\text{Fe}_y\text{OOH}$ -KOH (iron ions) is consistent with NC/ $\text{Ni}_x\text{Fe}_y\text{OOH}$ -KOH-pure (iron ions free), and superior to  $\text{Ni}_x\text{Fe}_y\text{OOH}$ -KOH (iron ions). This indicates a weak influence of iron ions, while NC owns a significant activity enhancement effect. Upon further comparison of the LSVs of four different electrodes: NC/NiOOH-KOH (iron ions), NC/ $\text{Ni}_x\text{Fe}_y\text{OOH}$ -KOH (iron ions), NC/NiOOH-KOH-pure (iron ions free), and NC/ $\text{Ni}_x\text{Fe}_y\text{OOH}$ -KOH-pure (iron ions free), the activity of the electrodes can be ranked as follows: NC/ $\text{Ni}_x\text{Fe}_y\text{OOH}$ -KOH (iron ions) = NC/ $\text{Ni}_x\text{Fe}_y\text{OOH}$ -KOH-pure (iron ions free), NC/NiOOH-KOH (iron ions) = NC/NiOOH-KOH (iron ions free), and NC/ $\text{Ni}_x\text{Fe}_y\text{OOH}$ -KOH (iron ions) > NC/NiOOH-KOH (iron ions). This indicates that iron ions have minimal effect, while lattice iron significantly enhances the activity of the NC/ $\text{Ni}_x\text{Fe}_y\text{OOH}$  electrode. Finally, by comparing the LSVs of  $\text{Ni}_x\text{Fe}_y\text{OOH}$ -KOH (iron ions) and NiOOH-KOH-pure (iron ions) electrodes, it can be observed that the activity of  $\text{Ni}_x\text{Fe}_y\text{OOH}$ -KOH (iron ions) is significantly superior to NiOOH-KOH-pure (iron ions). This further confirms the enhanced activity effect of lattice iron. In summary, it can be concluded that both NC and lattice iron have the advantages of enhancing the activity of the NC/ $\text{Ni}_x\text{Fe}_y\text{OOH}$  or  $\text{Ni}_x\text{Fe}_y\text{OOH}$  electrode. The significant difference in activity between impurity iron and lattice iron can be attributed to the following reasons. Firstly, iron ions in the electrolyte participate in the surface of NiOOH/ $\text{Ni}_x\text{Fe}_y\text{OOH}$  and gradually form aggregates of high-valence  $\text{FeO}_x$ . However, high-valence  $\text{FeO}_x$  is highly unstable and prone to leaching of iron. This results in a rapid decline in OER activity [35]. Secondly, the lattice iron in NC/ $\text{Ni}_x\text{Fe}_y\text{OOH}$  or  $\text{Ni}_x\text{Fe}_y\text{OOH}$  adapts to the strong oxidative environment imposed by the rapid reconstruction of the initial NiFe-MOF under high potentials. This not only enhances OER performance but also prevents activity decay caused by Fe leakage under industrial-scale high-current conditions [36]. Rhodamine B (Rh B) dyes are commonly used as molecular probes for evaluating the surface properties and adsorption capabilities of materials [37]. Next, we use Rh B as a molecular probe to verify the suc-

successful synthesis of NC. By comparing the UV-vis absorbance spectra of different mixtures (NC/(high purity KOH+Rh B) vs. high purity KOH+Rh B), the absorbance of NC/(high purity KOH+Rh B) is significantly reduced (Figure 2d, Table S2); this indicates that the CV activation method is feasible for synthesizing NC. After 200 cycles of CV activation, the characteristic peaks of derivative also show an amorphous structure in the XRD spectra (Figure S1b,c). Further FTIR characterizations (Figure S1e) show the same result. That is, NiFe-MOFs lose their ligands and reconstitute to NC/Ni<sub>x</sub>Fe<sub>y</sub>OOH. Unlike Ni<sub>x</sub>Fe<sub>y</sub>OOH, the Raman spectra of NC/Ni<sub>x</sub>Fe<sub>y</sub>OOH (Figure 2e) show only the stronger characteristic peaks of NiOOH appear at 475 and 554 cm<sup>-1</sup>. Compared with NC/Ni<sub>x</sub>Fe<sub>y</sub>OOH, the Raman spectra of Ni<sub>x</sub>Fe<sub>y</sub>OOH (Figure S1d) also show the typical characteristic peaks of NiOOH appear at 475 and 554 cm<sup>-1</sup>, in addition, there are weak characteristic peaks of NiFe-MOF at 779, 1080, and 1502 cm<sup>-1</sup>, suggesting that NiFe-MOF is not completely reconstructed to Ni<sub>x</sub>Fe<sub>y</sub>OOH [28,29]. These results indicate that trace NC (~0.4 ppm, Table S2) can accelerate the reconfiguration of NiFe-MOF to highly active NC/Ni<sub>x</sub>Fe<sub>y</sub>OOH. In addition, X-ray photoelectron spectroscopy (XPS) was further employed to investigate the surface elemental compositions and electronic states of the samples. As shown in Figure S10a, the XPS survey spectra on NiFe-MOF, Ni<sub>x</sub>Fe<sub>y</sub>OOH, NC/Ni<sub>x</sub>Fe<sub>y</sub>OOH surface confirm the presence of C, O, S, Ni, and Fe elements; which is consistent with the results of EDS spectrum (Figure S3a–c). High-resolution XPS spectra of Ni 2p, Fe 2p, and S 2p were presented in Figure S10b–d, respectively. The binding energy values of Ni 2p of NiFe-MOF show four major peaks, corresponding to Ni<sup>2+</sup> (855.9/873.5 eV), and their corresponding satellite peaks (identified as “Sat”, Figure S10d) [24]. Notably, the Ni 2p of Ni<sub>x</sub>Fe<sub>y</sub>OOH can be fitted into three pairs of peaks, these peaks are assigned to Ni<sup>3+δ</sup> (856.4/873.7 eV), Ni<sup>2+</sup> (855.4/872.7 eV), and satellite peaks (861.5/879.5 eV), respectively (Figure S10d) [38]. The appearance of Ni<sup>3+δ</sup> signals in Ni<sub>x</sub>Fe<sub>y</sub>OOH is in sharp contrast with NiFe-MOF; which further proves the formation of the target Ni<sub>x</sub>Fe<sub>y</sub>OOH. Compared with Ni<sub>x</sub>Fe<sub>y</sub>OOH, the Ni 2p<sub>3/2</sub> peak in the XPS spectrum of NC/Ni<sub>x</sub>Fe<sub>y</sub>OOH positively shifts about 0.2 eV (Figure S10d). This tendency suggests that the average valence state of Ni species in NC/Ni<sub>x</sub>Fe<sub>y</sub>OOH is in a higher oxidation state (Ni<sup>3+δ</sup>). Figure S10b shows the high-resolution spectrum of Fe 2p, in which the peaks of NiFe-MOF in Fe 2p spectrum at 709.3, 722.9, and 714.2 eV correspond to Fe<sup>2+</sup> and Fe<sup>3+</sup>, respectively [22,39]. This indicates that some Fe<sup>3+</sup> ions are reduced to Fe<sup>2+</sup> species, while Ni atoms of NF are oxidized to Ni<sup>2+</sup> species [38]. Analogously, compared with NiFe-MOF, the Fe<sup>3+</sup> 2p<sub>3/2</sub> peak of Ni<sub>x</sub>Fe<sub>y</sub>OOH and NC/Ni<sub>x</sub>Fe<sub>y</sub>OOH negatively shifts about 0.9 eV and 0.6 eV, respectively; which indicates that the synergistic effects of Ni-Fe in the as-prepared metal oxyhydroxides [40]. Next, the XPS of S 2p<sub>3/2</sub> at 164.1 eV and S 2p<sub>1/2</sub> at 165.3 eV indicate the thiophene-S chemical bond in the NiFe-MOF (Figure S10c) [24]. However, the thiophene-S of NC/Ni<sub>x</sub>Fe<sub>y</sub>OOH shows weaker characteristic peaks than Ni<sub>x</sub>Fe<sub>y</sub>OOH. In addition, a new peak located at 168.7 eV is clearly identified, corresponding to S-O in SO<sub>4</sub><sup>2-</sup> [41]. It was further indicated that NiFe-MOF lost a large number of ligands after CV activation, and thus reconstituted into NC/Ni<sub>x</sub>Fe<sub>y</sub>OOH. Next, the morphology of NC/Ni<sub>x</sub>Fe<sub>y</sub>OOH was also observed by SEM. Similar to Ni<sub>x</sub>Fe<sub>y</sub>OOH, the NC/Ni<sub>x</sub>Fe<sub>y</sub>OOH has a complete honeycomb structure and a uniform distribution of elements (Figures S3c and S11). According to SEM (Figure S11), TEM (Figures 3a–f and S13), and AFM (Figure S12), the as-prepared NC/Ni<sub>x</sub>Fe<sub>y</sub>OOH honeycomb consists of quasi-one-dimensional (or two-dimensional) ribbons with average dimensions of 32 nm in thickness, 300 nm in width, and tens of micrometers in length. In addition, the NC/Ni<sub>x</sub>Fe<sub>y</sub>OOH honeycomb owns hierarchical porosity composed of macropores around 300 μm originating from NF substrates and open pores around hundreds of nanometers to tens of micrometers formed by adjacent nanoribbons. The difference is that the C content (14.2 At%) of NC/Ni<sub>x</sub>Fe<sub>y</sub>OOH is lower than Ni<sub>x</sub>Fe<sub>y</sub>OOH (20 At%) (Figure S4b,c). It is further confirmed that the NC can accelerate the reconfiguration of NiFe-MOF to highly active NC/Ni<sub>x</sub>Fe<sub>y</sub>OOH. The HRTEM of NC/Ni<sub>x</sub>Fe<sub>y</sub>OOH (Figure 3c–e) also reveals a lattice spacing of 0.21 nm, corresponding to the (210) plane of NiOOH [30]. Furthermore, the selected area electron diffraction (SAED) pattern of NC/Ni<sub>x</sub>Fe<sub>y</sub>OOH

in Figure 3b shows well-defined diffraction rings, which are indexed to the (011), (210), (102) planes of NiOOH (PDF#27-0956) and (222) planes of NiO (PDF#73-1519). Combining the above multiple characterization test results, it can be specified that the derivative of NiFe-MOF is NC/Ni<sub>x</sub>Fe<sub>y</sub>OOH.

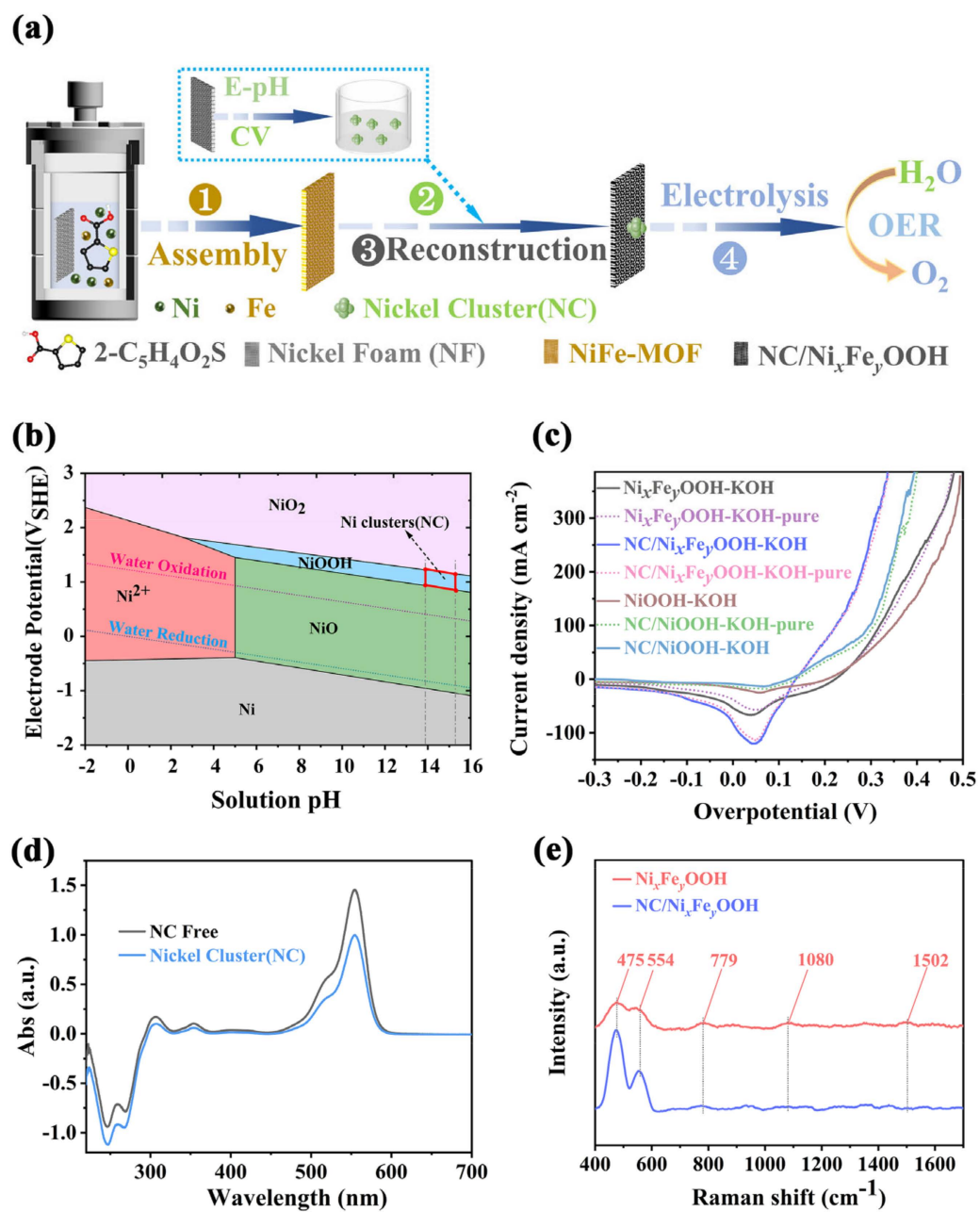


**Figure 2.** (a) Schematic illustration for the synthesis procedures of NC/Ni<sub>x</sub>Fe<sub>y</sub>OOH; (b) Pourbaix diagram of the Ni-water system; (c) influence of impurity iron in KOH electrolyte; (d) the UV-vis absorption spectra for Rh B in NC/KOH electrolyte; (e) Raman spectra of NC/Ni<sub>x</sub>Fe<sub>y</sub>OOH and Ni<sub>x</sub>Fe<sub>y</sub>OOH.

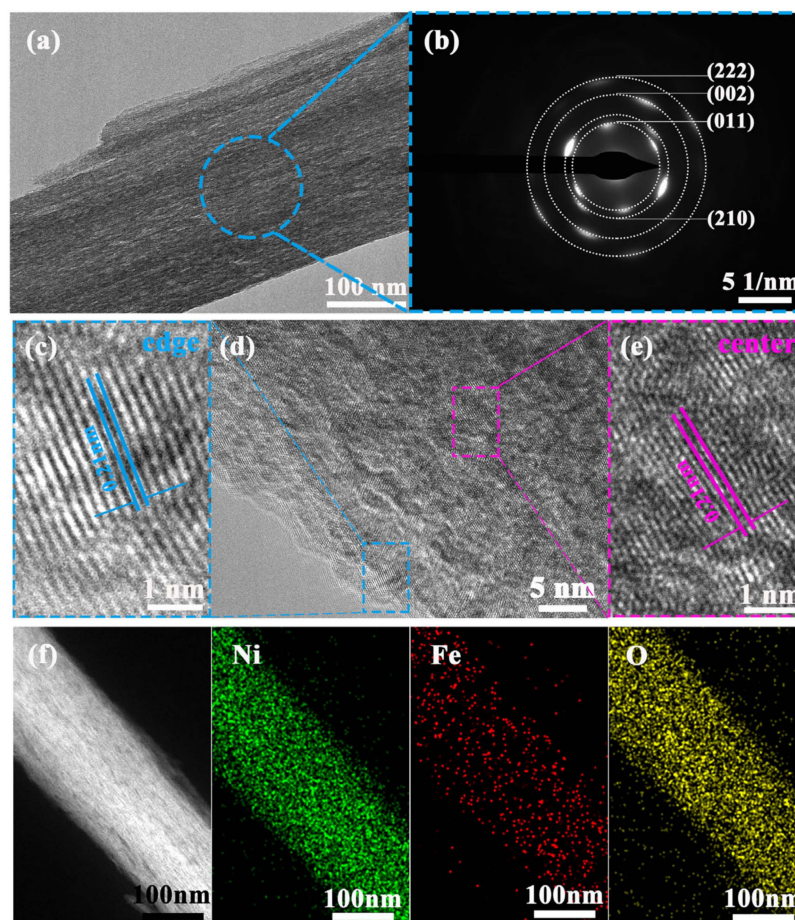


**Figure 3.** TEM characterizations of NC/Ni<sub>x</sub>Fe<sub>y</sub>OOH: (a) TEM image, (b) SAED image, (c–e) HRTEM image, (f) EDS mapping.

### 2.3. Electrocatalytic Performance of NC/Ni<sub>x</sub>Fe<sub>y</sub>OOH Catalyst

The electrochemical measurements of the NC/Ni<sub>x</sub>Fe<sub>y</sub>OOH were carried out with mechanical stirring (500 rpm) to avoid the accumulation of O<sub>2</sub> bubbles on the electrode [6,42]. Similar to seawater, SAW contains a large number of chloride ions, and calcium and magnesium ions. Therefore, it is easy for this to cause electrode blockage or corrosion, resulting in catalyst poisoning or falling off (Figure 1b, Table S1). Some necessary measures should be taken to reduce its negative effects. Adjusting the pH value of the solution to strong alkaline conditions can effectively inhibit the competitive chlorine evolution reaction, thus improving the activity and stability of the catalyst in seawater [6]. In this work, the obtained SAW is treated as follows. Firstly, the SAW obtained from a saline–alkali drainage canal in Alaer, Xinjiang had been simply filtered by using filter paper to remove impurities such as sediments and algae. Then, an appropriate amount of KOH solution is added to the SAW, mixed evenly and left for several hours. After filtering the precipitates, the supernatant is used as the electrolyte for catalytic reaction. For comparison, when the volume fraction of NC/KOH in NC/(KOH+SAW) mixed electrolyte was fixed at 50 vol%, several controlled experiments were carried out in NC/(1–6 M KOH+SAW). As shown in Figures 4a and S14, the NC/Ni<sub>x</sub>Fe<sub>y</sub>OOH operated in NC/(4 M KOH+SAW) electrolyte displays the optimum catalytic activity than other samples (such as IrO<sub>2</sub>, pristine NiFe-MOF, NF, etc.), only requiring an overpotential of 149 mV to attain the current density of 10 mA cm<sup>-2</sup>. The control sample of Ni<sub>x</sub>Fe<sub>y</sub>OOH operated in 4 M KOH+SAW electrolyte owns a higher overpotential of 233 mV@ 10 mA cm<sup>-2</sup>; this indicates a significantly enhanced OER performance upon the introduction of NC. In addition, to further confirm the NC enhancement activity effect, a series of control experiments were carried out in KOH+SAW electrolyte (NC free). Compared with Figures S14 and S15, it can be clearly observed that the overpotentials of

NC/Ni<sub>x</sub>Fe<sub>y</sub>OOH catalysts operated in NC/(1–6 M KOH+SAW) are significantly lower than that of the contrast samples (Ni<sub>x</sub>Fe<sub>y</sub>OOH operated in 1–6 M KOH+SAW), respectively. Obviously, the NC/Ni<sub>x</sub>Fe<sub>y</sub>OOH catalyst operated in NC/(4 M KOH+SAW) electrolyte also has lower overpotentials at other current densities of all catalysts operated in NC/(1–3, 5–6 M KOH+SAW) and 1–6 M KOH+SAW electrolyte, respectively (Figures S14b and S15d). As well as these, LSV curves recorded by sweeping from low to high potentials (positive sweep, Figures S14a and S15a) also show similar results. The NC enhancement activity effect also can be observed by Figure S15c, the performance of NC/Ni<sub>x</sub>Fe<sub>y</sub>OOH operated in NC/(4 M KOH+SAW) electrolyte is always better than Ni<sub>x</sub>Fe<sub>y</sub>OOH operated in 4 M KOH+SAW electrolyte under the same number of CV. This value is superior to most transition metal-based catalysts operated in seawater electrolyte (Table S3). To quantify the kinetic rate of the electrocatalytic reaction, the OER activities of NC/Ni<sub>x</sub>Fe<sub>y</sub>OOH and other control samples are also verified by Tafel plots (Figure 4b). The results indicate that NC/Ni<sub>x</sub>Fe<sub>y</sub>OOH catalyst operated in NC/(4 M KOH+SAW) electrolyte shows a much smaller Tafel slope of 47.4 mV dec<sup>-1</sup> than other contrast samples (67.2 mV dec<sup>-1</sup> of NC/(1 M KOH+SAW) vs. 73.9 mV dec<sup>-1</sup> of NC/(2 M KOH+SAW) vs. 77.5 mV dec<sup>-1</sup> of NC/(3 M KOH+SAW) vs. 61.8 mV dec<sup>-1</sup> of NC/(5 M KOH+SAW) vs. 81.7 mV dec<sup>-1</sup> of NC/(6 M KOH+SAW). Electrochemical surface area (ECSA) refers to the effective surface area of an electrode that participates in electrochemical reactions. A larger ECSA allows for more active sites where reactions can take place, leading to enhanced electrode kinetics and improved electrochemical performance. Electrochemical impedance spectroscopy (EIS) is a technique used to characterize the electrochemical behavior of a system by measuring its impedance response to an applied alternating current signal over a range of frequencies. It provides valuable information about the electrical properties and processes occurring at the electrode–electrolyte interface. Therefore, the ECSA (or C<sub>dl</sub>) and EIS of the above electrodes have been investigated. When the volume fractions of NC/KOH solution were fixed at 50%, the NC/Ni<sub>x</sub>Fe<sub>y</sub>OOH operated in NC/(4 M KOH+SAW) mixed electrolyte in Figure 4c exhibits a C<sub>dl</sub> value of 2.58 mF cm<sup>-2</sup>; this is noticeably larger than those of NC/Ni<sub>x</sub>Fe<sub>y</sub>OOH operated in NC/(1 M KOH+SAW, 1.9 mF cm<sup>-2</sup>), NC/(2 M KOH+SAW, 2.17 mF cm<sup>-2</sup>), NC/(3 M KOH+SAW, 2.17 mF cm<sup>-2</sup>), NC/(5 M KOH+SAW, 2.06 mF cm<sup>-2</sup>), and NC/(6 M KOH+SAW, 1.89 mF cm<sup>-2</sup>), respectively. In addition, based on the equivalent circuit in EIS analyses (Figure 4d, Table S4) [43], the charge-transfer resistance (R<sub>ct</sub>) of NC/Ni<sub>x</sub>Fe<sub>y</sub>OOH operated in NC/(4 M KOH+SAW) is calculated to be 0.29 Ω, which is much smaller than NC/Ni<sub>x</sub>Fe<sub>y</sub>OOH operated in NC/(1 M KOH+SAW, 44.75 Ω), NC/(2 M KOH+SAW, 18.79 Ω), NC/(3 M KOH+SAW, 0.79 Ω), NC/(5 M KOH+SAW, 9.13 Ω), and NC/(6 M KOH+SAW, 14.57 Ω), respectively. The results show a high mass/electron transfer coefficient and rapid electrocatalytic kinetics of NC/Ni<sub>x</sub>Fe<sub>y</sub>OOH operated in NC/(4 M KOH+SAW). On one hand, according to the Pourbaix diagram of Ni-water system [32], it can be observed that the reaction potentials for synthesizing nickel cluster dispersions vary with different concentrations of KOH. When the potential is fixed, different valence states of nickel cluster dispersions may be synthesized under different KOH concentrations, resulting in differences in catalytic activity. On the other hand, the concentration of KOH electrolyte can have a significant impact on the dispersion effect, catalytic activity, and electrochemical stability of nickel–metal cluster dispersions (NCs). Generally, higher KOH concentrations can promote the uniform dispersion of metal clusters, while lower concentrations may lead to nickel clusters aggregation or precipitation. An appropriate concentration of KOH can provide the required alkaline environment, facilitating the adsorption and reaction of oxygen species, thereby enhancing the catalytic activity. However, excessively high or low KOH concentrations may have a negative impact on the catalyst's activity. Higher concentrations of KOH can lead to more vigorous oxidation processes, accelerating the oxidation or corrosion of nickel clusters. Therefore, it is necessary to strike a balance in KOH concentration to achieve both good electrochemical stability and activity [1,44,45]. Different concentrations of KOH electrolyte exhibit variations in ionic conductivity, activation energy, and viscosity; these consequently have a significant impact on the activity of

catalysts. The ionic conductivity of KOH electrolyte increases with higher concentrations, as more ions are available for conduction. However, as the concentration of KOH electrolyte continues to increase, there is typically a volcano-shaped trend between the conductivity and KOH concentration. This enhanced conductivity in suitable KOH electrolyte concentration allows for more efficient charge transfer at the catalyst-electrolyte interface, leading to improved catalytic activity. The activation energy, which represents the energy barrier for catalytic reactions, can be influenced by the concentration of KOH electrolyte. Changes in electrolyte concentration can alter the adsorption and reaction kinetics of species on the catalyst surface. This affects the activation energy required for the catalytic process. Optimal electrolyte concentrations can provide suitable reaction conditions, resulting in lower activation energies and enhanced catalytic activity. Additionally, the viscosity of the KOH electrolyte changes with the concentration. Higher viscosity can impede mass transport and diffusion processes, potentially reducing the accessibility of reactants to the catalyst surface and hindering catalytic reactions. Conversely, lower viscosity facilitates mass transport and can improve catalytic activity [44,45]. Therefore, it is important to consider the effects of KOH electrolyte concentration on ionic conductivity, activation energy, and viscosity when evaluating the activity of catalysts. According to the analysis of Tafel plots (Figure 4b), ECSA (Figure 4c) and EIS (Figure 4d), it can be concluded that the NC/ $\text{Ni}_x\text{Fe}_y\text{OOH}$  electrode in the NC/(4 M KOH+SAW) electrolyte exhibits the lowest impedance and Tafel values, as well as the maximum capacitance ( $C_{dl}$ ). Therefore, the NC/ $\text{Ni}_x\text{Fe}_y\text{OOH}$  electrode demonstrates the optimal activity in the NC/(4 M KOH+SAW) electrolyte.

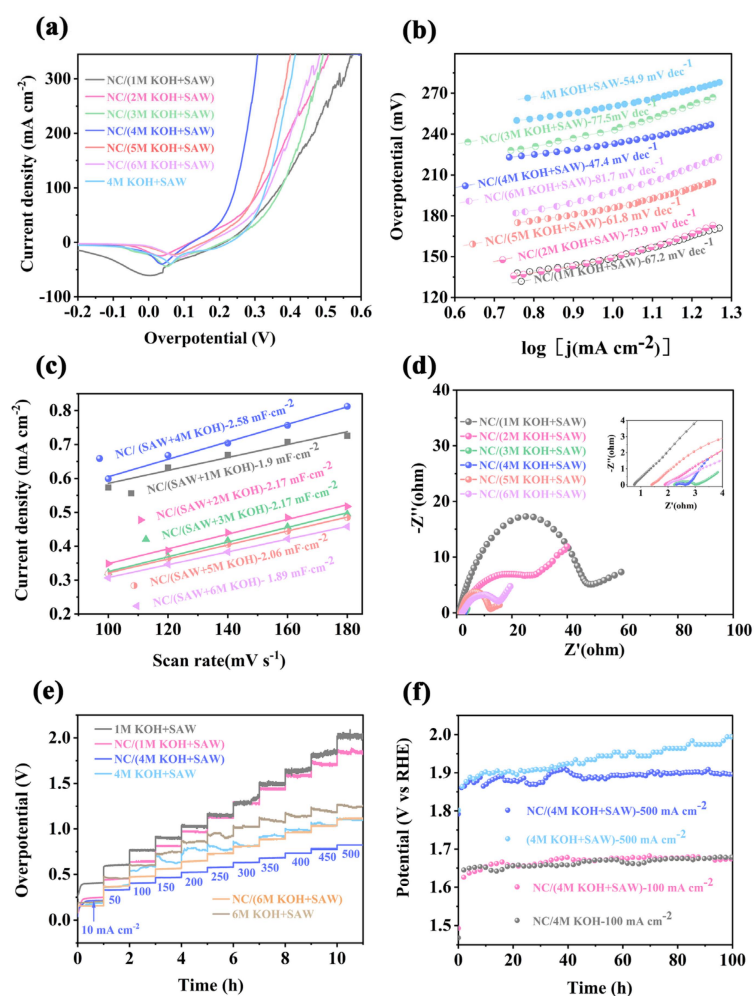


**Figure 4.** (a) The polarization curves for NC/ $\text{Ni}_x\text{Fe}_y\text{OOH}$  operated in NC/(1–6 M KOH+SAW); (b) Tafel slopes; (c) ECSA; (d) EIS of NC/ $\text{Ni}_x\text{Fe}_y\text{OOH}$  operated in NC/(1–6 M KOH+SAW); (e) multi-step E-t curves; (f) chronopotentiometry curves of NC/ $\text{Ni}_x\text{Fe}_y\text{OOH}$  without iR-compensation.

Further, when the NC/KOH solution concentration was fixed at 4 M, the activities of NC/Ni<sub>x</sub>Fe<sub>y</sub>OOH catalysts in different volume fraction (0–90 vol%) of NC/KOH solution operated in the NC/(KOH+SAW) or KOH+SAW mixed electrolyte had been operated. Firstly, according to Figures S16 and S17, the NC enhancement effect on NC/Ni<sub>x</sub>Fe<sub>y</sub>OOH catalyst was highlighted again, along with the volume fraction of NC/KOH range from 0% to 90% and the optimal volume fraction of KOH operated in the 4 M NC/(KOH+SAW) mixed electrolyte is also 50 vol%. On this basis, the ECSA and EIS of NC/Ni<sub>x</sub>Fe<sub>y</sub>OOH with different volume fractions of KOH were also studied. Figure S18 demonstrates that the maximum C<sub>dl</sub> of the three samples (2.15 mF cm<sup>-2</sup> @ 30 vol% vs. 2.58 mF cm<sup>-2</sup> @ 50 vol% vs. 2.18 mF cm<sup>-2</sup> @ 70 vol% KOH). Similarly, Figure S19 and Table S5 show that the NC/Ni<sub>x</sub>Fe<sub>y</sub>OOH catalyst operated in 50 vol% KOH of NC/(4 M KOH+SAW) mixed electrolyte owns a smaller R<sub>ct</sub> (0.29 Ω) than other catalysts operated in 50% and 70% volume fraction of KOH (48 Ω vs. 104.5 Ω). Through the above comparative analysis, it is fully demonstrated that the NC/Ni<sub>x</sub>Fe<sub>y</sub>OOH catalyst operated in 50 vol% KOH of NC/(4 M KOH+SAW) mixed electrolyte has the best catalytic performance. On this basis, the FE of NC/Ni<sub>x</sub>Fe<sub>y</sub>OOH, Ni<sub>0.5</sub>Fe<sub>0.5</sub>/Ni<sub>x</sub>Fe<sub>y</sub>OOH, Fe/Ni<sub>x</sub>Fe<sub>y</sub>OOH were identified by using a water drainage method (Figure S27); the NC/Ni<sub>x</sub>Fe<sub>y</sub>OOH has the highest catalytic efficiency (98.2% vs. 92.4% vs. 91.2%). It has again been proved that the introduction of trace NC significantly improves the performance of this system (Figures 2c and S27b).

Other than activities, stability is another important criterion for evaluating OER for practical applications. Chronopotentiometry is an electrochemical technique used to measure the potential changes at an electrode as a function of time under a constant current. Accordingly, chronopotentiometry measurements were performed to investigate dynamic response and the long-term stability of NC/Ni<sub>x</sub>Fe<sub>y</sub>OOH operated in different KOH concentration. The multi-step E-t curves, with the current density increasing from 10 to 500 mA cm<sup>-2</sup>, are shown in Figure 4e. It can be seen that the applied potentials of NC/Ni<sub>x</sub>Fe<sub>y</sub>OOH operated in NC/(1 M KOH+SAW), NC/(4 M KOH+SAW), and NC/(6 M KOH+SAW) remain relatively stable without appreciable variations at different current densities. In addition, when the current density increases from 10 to 250 mA cm<sup>-2</sup>, the applied potentials of Ni<sub>x</sub>Fe<sub>y</sub>OOH operated in 1 M KOH+SAW also keeps a small fluctuation range; however, when the current density exceeds 250 mA cm<sup>-2</sup>, the Ni<sub>x</sub>Fe<sub>y</sub>OOH operated in 1 M KOH+SAW shows a big potential fluctuation. Both of the Ni<sub>x</sub>Fe<sub>y</sub>OOH operated in 4 M KOH+SAW and 6 M KOH+SAW exhibit large voltage oscillations in all current density range (10–500 mA cm<sup>-2</sup>). Notably, the NC/Ni<sub>x</sub>Fe<sub>y</sub>OOH operated in NC/(4 M KOH+SAW) shows a lower overpotential in comparison with that of the other samples. The above studies show that the introduction of NC significantly improves the activity of the NC/Ni<sub>x</sub>Fe<sub>y</sub>OOH catalyst and maintains a high stability. In other words, the NC/Ni<sub>x</sub>Fe<sub>y</sub>OOH may have a self-healing ability in the suitable electrolyte (NC/(4 M KOH+SAW) or NC/(6 M KOH+SAW) even at high current density (up to 500 mA cm<sup>-2</sup>). In order to further verify the self-healing ability of the NC/Ni<sub>x</sub>Fe<sub>y</sub>OOH catalyst, the measurements of long-term stability of NC/Ni<sub>x</sub>Fe<sub>y</sub>OOH have been taken. According to Figure 4f, it can be seen that the NC/Ni<sub>x</sub>Fe<sub>y</sub>OOH catalysts can maintain good stability (the activity is nearly 100%) for 100 h @100 mA cm<sup>-2</sup> and almost the same overpotential operated in both NC/4 M KOH and NC/(4 M KOH+SAW) electrolyte. When the current density is increased to industrial level (≥500 mA cm<sup>-2</sup>), the chronopotentiometry at 500 mA cm<sup>-2</sup> of the NC/Ni<sub>x</sub>Fe<sub>y</sub>OOH electrode still remains highly stable with negligible increase (the activity attenuation is less than 3%) throughout 100 h of continuous operation in NC/(4 M KOH+SAW) electrolyte. The corresponding LSV curve (Figure S20) of NC/Ni<sub>x</sub>Fe<sub>y</sub>OOH without iR compensation after the 100 h durability test shows that approximately 98% of the activity is retained, demonstrating excellent OER durability. However, when the electrolyte was replaced by 4 M KOH+SAW (NC free), the activity of Ni<sub>x</sub>Fe<sub>y</sub>OOH catalyst continued to decay over time. After 100 h continuous testing at 500 mA cm<sup>-2</sup>, the activity attenuation is more than 10%, and this activity decay trend may continue to increase with the extension of reaction time. Moreover, we examined the surface morphology and structure

of the NC/Ni<sub>x</sub>Fe<sub>y</sub>OOH catalyst after stability testing operated in NC/(4 M KOH+SAW) electrolyte. According to the results in Figures S21–S24, the NC/Ni<sub>x</sub>Fe<sub>y</sub>OOH catalyst still remains in a tough honeycomb structure, with a uniform distribution of elements, a similar crystal structure, and highly similar element valence states of Ni, Fe. It can be seen that the NC not only significantly enhances the catalytic activity of NC/Ni<sub>x</sub>Fe<sub>y</sub>OOH, but also has the ability to promote rapid self-healing of the NC/Ni<sub>x</sub>Fe<sub>y</sub>OOH electrode even under high current density. Finally, we set up a two-electrode electrolyzer in a liquid flow electrolytic cell for overall SAW splitting operated in NC/(4 M KOH+SAW) (Figure S25). The NC/Ni<sub>x</sub>Fe<sub>y</sub>OOH electrode (OER) was coupled with HER catalyst of commercial Pt/C electrode supported on nickel foam, and the NC/Ni<sub>x</sub>Fe<sub>y</sub>OOH || Pt/C can keep stability and activity for 100 h at 500 mA cm<sup>-2</sup>. The faradaic efficiency (FE) for overall SAW splitting was identified by directly measuring the amount of generated H<sub>2</sub>/O<sub>2</sub> bubbles through a water drainage method [42]. The products of H<sub>2</sub> and O<sub>2</sub> with a molar ratio approaching 2:1, and the experimental gas amounts are in good agreement with the theoretical results, demonstrating a 95.2% faradaic efficiency.

#### 2.4. Possible Reasons for the Self-Healing NC/Ni<sub>x</sub>Fe<sub>y</sub>OOH Catalyst

Before studying the self-healing mechanism, it is necessary to determine the catalytic reaction type of the synthesized NC, as they are uniformly dispersed in the KOH electrolyte. That is, it is necessary to determine whether the enhanced catalytic effect of NC belongs to homogeneous catalysis or heterogeneous catalysis. Therefore, a set of verification experiments were designed. As shown in Figure 5a, first, carbon rod with very poor activity was selected as a working electrode for OER. Compared with the LSVs of carbon rod electrode operated in 4 M KOH+SAW electrolyte and NC/(4 M KOH+SAW) electrolyte, respectively, there is no activity difference. On this basis, disperse the NiFe-MOF powder separately operated in 4 M KOH+SAW electrolyte and NC/(4 M KOH+SAW) electrolyte, followed by thorough CV activation. Then, use a carbon rod as the working electrode once again for OER. The results indicate that there is still no difference in performance between the two. Notably, when the carbon rod is replaced with Ni<sub>x</sub>Fe<sub>y</sub>OOH and NC/Ni<sub>x</sub>Fe<sub>y</sub>OOH electrode, the activities of Ni<sub>x</sub>Fe<sub>y</sub>OOH and NC/Ni<sub>x</sub>Fe<sub>y</sub>OOH electrode show a significant difference, which operated in 4 M KOH+SAW electrolyte and NC/(4 M KOH+SAW) electrolyte, respectively. The above research indicates that the NC dispersed in the electrolyte cannot undergo homogeneous catalytic reactions independently. They need to be adsorbed onto an appropriate supported catalyst (Ni<sub>x</sub>Fe<sub>y</sub>OOH or NC/Ni<sub>x</sub>Fe<sub>y</sub>OOH) to exhibit enhanced catalytic activity. In electrolytic water, mechanical stirring can usually increase the convection and diffusion effect between gas products (H<sub>2</sub>/O<sub>2</sub>) and reactive ions (H<sup>+</sup>/OH<sup>-</sup>) in the solution, and improve the rate and efficiency of product transfer [42,46]. Figures 5b and S28 show that NC/Ni<sub>x</sub>Fe<sub>y</sub>OOH catalyst operated in 4 M KOH+SAW electrolyte has the least activity of all catalysts and when the speed is increased from 0 to 500 rpm, its performance does not change. Unlike Ni<sub>x</sub>Fe<sub>y</sub>OOH catalyst, NC/Ni<sub>x</sub>Fe<sub>y</sub>OOH catalyst in a static (0 rpm) NC/(4 M KOH+SAW) electrolyte shows good activity, when the speed increased to 500 rpm, the activity of NC/Ni<sub>x</sub>Fe<sub>y</sub>OOH catalyst is further enhanced, but when the speed is increased to 800 rpm, the activity of NC/Ni<sub>x</sub>Fe<sub>y</sub>OOH catalyst does not change. This indicates that mechanical stirring is an important pathway to promote full contact of NC with NC/Ni<sub>x</sub>Fe<sub>y</sub>OOH supported catalyst. Thus, the activity of NC/Ni<sub>x</sub>Fe<sub>y</sub>OOH catalyst is improved by a simple mechanical stirring. The LSVs of NC/Ni<sub>x</sub>Fe<sub>y</sub>OOH catalyst after different CV cycles have been obtained (Figure 5c). It can be seen that the activity of NC/Ni<sub>x</sub>Fe<sub>y</sub>OOH operated in NC/(4 M KOH+SAW) significantly declines after 1 CV cycle when the mechanical stirring speed is 0 r/min (denoted as NC/Ni<sub>x</sub>Fe<sub>y</sub>OOH-0-1). Then, the degraded NC/Ni<sub>x</sub>Fe<sub>y</sub>OOH-0-1 electrode is placed in a flowing NC/(4 M KOH+SAW) electrolyte with a speed of 500 r/min for 1 CV (denoted as NC/Ni<sub>x</sub>Fe<sub>y</sub>OOH-500-1), the activity of NC/Ni<sub>x</sub>Fe<sub>y</sub>OOH-500-1 significantly improves. When the recovered NC/Ni<sub>x</sub>Fe<sub>y</sub>OOH-500-1 electrode was put into the NC/(4 M KOH+SAW) electrolyte at the speed of 0 r/min for 10 CV, the performance of NC/Ni<sub>x</sub>Fe<sub>y</sub>OOH-500-1 declined again

(denoted as NC/Ni<sub>x</sub>Fe<sub>y</sub>OOH-0-10). Next, the degraded NC/Ni<sub>x</sub>Fe<sub>y</sub>OOH-0-10 electrode is placed in a flowing NC/(4 M KOH+SAW) electrolyte with a speed of 500 r/min for 10 CV (denote as NC/Ni<sub>x</sub>Fe<sub>y</sub>OOH-500-10); the activity of NC/Ni<sub>x</sub>Fe<sub>y</sub>OOH-500-10 electrode significantly improves again. A similar self-healing phenomenon can also be observed when the electrodes operate at 500 r/min for 100 CV. In conclusion, after the same CV operation in a flowing NC/(4 M KOH+SAW) electrolyte with a speed of 500 r/min, the activity of NC/Ni<sub>x</sub>Fe<sub>y</sub>OOH catalyst is significantly enhanced and consistently in a highly active state. The self-healing OER catalysts are a specific type of OER catalyst that continually regenerate themselves through an equilibrium process that occurs under the operating conditions. That is, the requirement for self-healing is that the dissolution and redeposition of catalytic centers must reach dynamic equilibrium at OER operational potentials [6,38,40,47]. In this work, the possible self-healing mechanism is proposed in Figure 5d. The metal oxidation process before catalysis alternates with the metal reduction process in the oxygen evolution reaction of NC/Ni<sub>x</sub>Fe<sub>y</sub>OOH. When the rates between metal oxidation ( $V_{\text{MOX}}$ ) and metal reduction ( $V_{\text{OER}}$ ) of NC/Ni<sub>x</sub>Fe<sub>y</sub>OOH reach a dynamic equilibrium, this oxidation-reduction process can be infinitely cycled, thereby achieving self-healing. Specifically, uniformly dispersed NC in the electrolyte plays a crucial role in achieving self-healing of NC/Ni<sub>x</sub>Fe<sub>y</sub>OOH catalyst. Several possible reasons have been proposed to explain the phenomenon of self-healing: (1) NC act as surface activators, they can effectively modulate the electronic properties of the NC/Ni<sub>x</sub>Fe<sub>y</sub>OOH catalyst and alter the local microenvironment, facilitating the rapid generation of high-valence nickel (Ni<sup>3+δ</sup>) during the reconstruction of NiFe-MOF, leading to a significant heterogeneous catalytic enhancement (Figures 2e, 5a, S10 and S15c) [48–50]. (2) Moreover, the NC dispersed in KOH+SAW electrolyte can adsorb a large amount of OH<sup>−</sup>. Then, under the mechanical stirring, NC loaded with a large amount of OH<sup>−</sup> are migrated to the surface of the supported catalyst (NC/Ni<sub>x</sub>Fe<sub>y</sub>OOH). During vigorous OER, highly active NC and high valence nickel (Ni<sup>3+δ</sup>) of NC/Ni<sub>x</sub>Fe<sub>y</sub>OOH can rapidly consume lots of OH<sup>−</sup> ions, resulting in a decrease in the OH<sup>−</sup> concentration at Fe sites and enhancing the stability of Fe sites in NC/Ni<sub>x</sub>Fe<sub>y</sub>OOH (Figures 4f, S4a–c, S21 and S24) [6,36]. (3) Extensive research has shown that most pristine OER electrocatalysts undergo dynamic and irreversible restructuring processes when subjected to oxidation potentials in alkaline media. This leads to the formation of transition metal-based oxyhydroxides (MOOH) as the actual catalytic species. Compared to directly synthesized MOOH, reconstructed MOOH typically exhibits superior OER activity and is more thermodynamically stable. A comprehensive understanding of surface reconstruction processes plays a crucial role in establishing a clear structure–composition–property relationship to pursue highly efficient electrocatalysts. Therefore, structural reconstruction has emerged as a promising strategy for enhancing the catalytic activity of electrocatalysts [51,52]. Hence, highly active NC and high CV potential (1.5–1.7 V vs. RHE) create a fast and strong oxidative environment for the reconstruction of NiFe-MOF, providing thermodynamic conditions for Fe to undergo adaptive strong oxidation. This effectively solves the issue of Fe segregation in NC/Ni<sub>x</sub>Fe<sub>y</sub>OOH during continuous high-intensity operation (Figures 4f, S4a–c, S15c, S21 and S24) [6,36,40,53]. (4) A large amount of Fe in NiFe-MOF also can indeed promote the formation of high-valence nickel (Ni<sup>3+δ</sup>) during NiFe-MOF reconstruction and the regeneration of NC (Figures 2b,c,e, 5c, S4, S6 and S10d) [50]; thus, the advantages of nickel–iron synergism are fully demonstrated [40]. The combined action of (1), (2), (3), and (4) can greatly enhance the rate of high-valence nickel formation ( $V_{\text{MOX}}$ ), bringing it closer to the consumption rate ( $V_{\text{OER}}$ ) (Figures 4f and 5c) [47], and thereby achieving dynamic equilibrium or self-healing. In addition to NC, other factors contribute to improving the activity and stability of NC/Ni<sub>x</sub>Fe<sub>y</sub>OOH catalyst, such as robust self-grown electrodes, hierarchical porous honeycomb structures, and strong alkaline environments (Figures 3e,f and S11) [54,55]. In summary, as long as the catalyst meets the conditions of uniform dispersion of metal clusters, appropriate electrolyte concentration, highly active and robust supported catalysts, as well as sufficient agitation, it can achieve excellent self-healing

performance. This provides another favorable approach for the industrial application of low-grade water electrolysis.

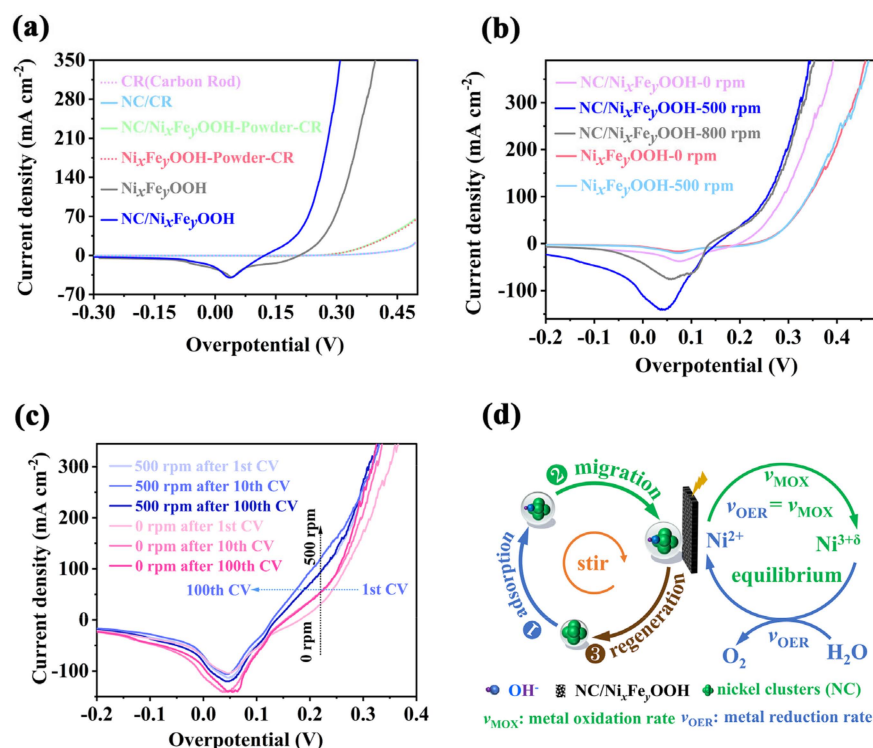


**Figure 5.** (a) Heterogeneous catalysis experiment; (b) the effect of mechanical stirring rate on the activity of NC/Ni<sub>x</sub>Fe<sub>y</sub>OOH, and Ni<sub>x</sub>Fe<sub>y</sub>OOH; (c) the effect of mechanical stirring on self-healing ability of NC/Ni<sub>x</sub>Fe<sub>y</sub>OOH; (d) possible self-healing schematic of NC/Ni<sub>x</sub>Fe<sub>y</sub>OOH.

### 3. Materials and Methods

#### 3.1. Chemicals

All chemicals were used as they were received from manufacturers. Please see the Supplementary Materials section for details.

#### 3.2. Synthesis of NiFe-MOFs

NiFe-MOFs were prepared according to our previous work [33]. The prepared NiFe-MOFs were used as the precursors to synthesize Ni<sub>x</sub>Fe<sub>y</sub>OOH and NC/Ni<sub>x</sub>Fe<sub>y</sub>OOH catalyst.

#### 3.3. Synthesis of Nickel Clusters (NC) and Iron Clusters and Nickel–Iron Clusters

Nickel clusters were synthesized by cyclic voltammetry (CV). Firstly, a piece of clean nickel foam (NF, 1 cm × 1 cm × 1.6 mm) was used as working electrode (graphite rod and Hg/HgO as counter, and reference electrode, respectively). Then, OER was tested in a three-electrode system in a single electrolytic cell with 1–6 mol/L (denoted as M) KOH aqueous solution (with 85% iR-compensation) under stirring; CV plots were recorded at a scan rate of 100 mV s<sup>-1</sup> from 1.8 to 2.0 V (vs. RHE) for 200 cycles. After the CV test of NF, NC uniformly distributed in 1 M KOH electrolyte was synthesized (denoted as NC/1 M KOH). Similar to the synthesis of NC/1 M KOH, the NC/2 M KOH, NC/3 M KOH, NC/4 M KOH, NC/5 M KOH and NC/6 M KOH were obtained using 2–6 M KOH as electrolyte, respectively. In addition, the synthesis of iron clusters and nickel–iron clusters is similar to the synthesis of NC but using iron foam and nickel–iron foam as working electrode, 4 M KOH as electrolyte, respectively.

### 3.4. Synthesis of $Ni_xFe_yOOH$ and $NC/Ni_xFe_yOOH$

Similar to the synthesis of NC,  $NC/Ni_xFe_yOOH$  electrode was obtained to reconstruct NiFe-MOF in NC/4 M KOH solution by CV at a scan rate of  $100\text{ mV s}^{-1}$  from 1.5 to 1.7 V (vs. RHE). Synthesis of  $Ni_xFe_yOOH$  catalyst was similar to  $NC/Ni_xFe_yOOH$  electrode but using 4 M KOH solution as electrolyte.

### 3.5. Characterizations

Details of this section are supplied in the Supplementary Materials.

### 3.6. Electrochemical Measurements

Details of this section are supplied in the Supplementary Materials.

## 4. Conclusions

In conclusion, we propose a method that is simple, efficient, and versatile to be used for the preparation of a series clusters (NC, Fe, and  $Ni_{0.5}Fe_{0.5}$ ) to enhance active catalysts by the simple cyclic voltammetry in alkaline electrolyte. These synthetic electrodes have demonstrated excellent structural advantages for electrocatalytic reactions. For example, strong adhesion between the active material and the substrate, reconstructed from NiFe-MOF self-supporting electrode by cyclic voltammetry; the hierarchical porosity of the honeycomb structure for fast diffusion of electrolytes and gases, and excellent electrical conductivity for efficient charge transport. Importantly, benefitting from strong synergy between Ni clusters and robust supported catalyst ( $NC/Ni_xFe_yOOH$ ), the  $NC/Ni_xFe_yOOH$  catalyst has an ultra-low overpotential of  $149\text{ mV}@10\text{ mA cm}^{-2}$ , 98.2% FE, durable stability of 100 h at  $500\text{ mA cm}^{-2}$  (activity attenuation < 3%), and remarkable self-healing properties for OER in low-grade saline-alkali water. The self-healing catalyst may become one of the development directions of the next generation of high-efficiency electrocatalyst.

**Supplementary Materials:** The following supporting information can be downloaded at: <https://www.mdpi.com/article/10.3390/catal14010081/s1>, Figure S1: XRD, FTIR, Raman, SEM, TEM of NiFe-MOF and reconstructions; Figure S2: Morphology characterizations of NiFe-MOF; Figure S3: SEM Mappings of NiFe-MOF,  $Ni_xFe_yOOH$ ,  $NC/Ni_xFe_yOOH$ ; Figure S4: SEM EDS of NiFe-MOF,  $Ni_xFe_yOOH$ ,  $NC/Ni_xFe_yOOH$ ; Figure S5: The activities of  $Ni_xFe_yOOH$  in KOH and saline-alkali water (SAW), respectively; Figure S6: Influence of impurity iron in KOH electrolyte, sweeping from low to high potentials; Figure S7: The activities of  $Ni_xFe_yOOH$  in different concentration of KOH with homogeneous distributed NC; Figure S8: The effect of synthesizing nickel clusters (NC) with different CV activation potentials on the activity of  $Ni_xFe_yOOH$  catalyst; Figure S9: The effect of synthesizing metal clusters (NC, Fe,  $Ni_{0.5}Fe_{0.5}$ ) with different cyclic voltammetry (CV) activation circles on the activity of  $Ni_xFe_yOOH$  catalyst; Figure S10: XPS spectra of NiFe-MOF,  $Ni_xFe_yOOH$ , and  $NC/Ni_xFe_yOOH$ ; Figure S11: SEM images of  $NC/Ni_xFe_yOOH$ ; Figure S12: AFM image of  $NC/Ni_xFe_yOOH$ ; Figure S13: TEM Mappings of  $NC/Ni_xFe_yOOH$ ; Figure S14: The activities of  $Ni_xFe_yOOH$  in  $NC/(1-6\text{ M KOH}+\text{saline-alkali water (SAW)})$  mixed electrolyte; Figure S15: The activities of  $Ni_xFe_yOOH$  in  $1-6\text{ M KOH}+\text{saline-alkali water (SAW)}$  mixed electrolyte; Figure S16: The activities of  $Ni_xFe_yOOH$  in  $NC/(4\text{ M KOH}+\text{saline-alkali water (SAW)})$  mixed electrolyte with different volume fraction of NC/KOH; Figure S17: The activities of  $Ni_xFe_yOOH$  in  $4\text{ M KOH}+\text{saline-alkali water (SAW)}$  mixed electrolyte with different volume fraction of KOH; Figure S18: Cdl of  $Ni_xFe_yOOH$  in  $NC/(4\text{ M KOH}+\text{saline-alkali water (SAW)})$  mixed electrolyte with different volume fraction of NC/KOH; Figure S19: Nyquist plots of  $Ni_xFe_yOOH$  in  $NC/(4\text{ M KOH}+\text{saline-alkali water (SAW)})$  mixed electrolyte with different volume fraction of KOH; Figure S20: The activities of  $NC/Ni_xFe_yOOH$  before and after 100 h chronopotentiometry measurement at  $500\text{ mA cm}^{-2}$ ; Figure S21: The structure of  $NC/Ni_xFe_yOOH$  before and after 100 h chronopotentiometry measurement at  $500\text{ mA cm}^{-2}$ ; Figure S22: The FTIR spectra of  $NC/Ni_xFe_yOOH$  before and after 100 h chronopotentiometry measurement at  $500\text{ mA cm}^{-2}$ ; Figure S23: The XRD spectra of  $NC/Ni_xFe_yOOH$  before and after 100 h chronopotentiometry measurement at  $500\text{ mA cm}^{-2}$ ; Figure S24: The XPS spectra of  $NC/Ni_xFe_yOOH$  before and after 100 h chronopotentiometry measurement at  $500\text{ mA cm}^{-2}$ ; Figure S25: The overall water splitting per-

formance of NC/NixFeyOOH || Pt/C; Figure S26: The effect of synthesizing different clusters (NC) on the activity of NC/NixFeyOOH catalyst; Figure S27: Digital photograph of the equipment for measuring the volume of as-produced O<sub>2</sub> and FE spectrum; Figure S28: The effect of mechanical stirring rate on the activity of NC/NixFeyOOH; Table S1: ICP-MS analysis of saline-alkali water; Table S2: ICP-MS analysis of nickel clusters; Table S3: Comparison of seawater OER activities with recently reported transition metal base electrocatalysts; Table S4: EIS simulation of NC/NixFeyOOH in 1–6 M NC/KOH+saline-alkali water (SAW) mixed electrolyte. Table S5: EIS simulation of NC/NixFeyOOH in 4 M NC/KOH+saline-alkali water (SAW) mixed electrolyte with different vol% KOH. References [42,55–68] are cited in the Supplementary Materials.

**Author Contributions:** Methodology, investigation, writing original draft, visualization, H.W.; conceptualization, writing—review and editing, supervision, funding acquisition, S.C. All authors have read and agreed to the published version of the manuscript.

**Funding:** This research was funded by the financial support from the Jiangsu Natural Science Foundation (BK20230097), National Natural Science Foundation of China (92163124, 51888103 and 52006105) and Fundamental Research Funds for the Central Universities (30920041113 and 30921013103).

**Data Availability Statement:** The data presented in this study are available.

**Acknowledgments:** The authors thank Yue Chen from Shiyanjia Lab ([www.Shiyanjia.com](http://www.Shiyanjia.com), access since 15 January 2024) for the ICP and TEM measurements.

**Conflicts of Interest:** The authors declare no competing financial interests.

## References

1. Chatenet, M.; Pollet, B.G.; Dekel, D.R.; Dionigi, F.; Deseure, J.; Millet, P.; Braatz, R.D.; Bazant, M.Z.; Eikerling, M.; Staffell, I.; et al. Water Electrolysis: From Textbook Knowledge to the Latest Scientific Strategies and Industrial Developments. *Chem. Soc. Rev.* **2022**, *51*, 4583–4762. [[CrossRef](#)] [[PubMed](#)]
2. Fu, X.; Shi, R.; Jiao, S.; Li, M.; Li, Q. Structural Design for Electrocatalytic Water Splitting to Realize Industrial-Scale Deployment: Strategies, Advances, and Perspectives. *J. Energy Chem.* **2022**, *70*, 129–153. [[CrossRef](#)]
3. Zhao, J.; Zhang, J.J.; Li, Z.Y.; Bu, X.H. Recent Progress on NiFe-Based Electrocatalysts for the Oxygen Evolution Reaction. *Small* **2020**, *16*, e2003916. [[CrossRef](#)] [[PubMed](#)]
4. Yang, F.; Luo, Y.; Yu, Q.; Zhang, Z.; Zhang, S.; Liu, Z.; Ren, W.; Cheng, H.M.; Li, J.; Liu, B. A Durable and Efficient Electrocatalyst for Saline Water Splitting with Current Density Exceeding 2000 mA cm<sup>-2</sup>. *Adv. Funct. Mater.* **2021**, *31*, 2010367. [[CrossRef](#)]
5. Vorosmarty, C.J.; McIntyre, P.B.; Gessner, M.O.; Dudgeon, D.; Prusevich, A.; Green, P.; Glidden, S.; Bunn, S.E.; Sullivan, C.A.; Liermann, C.R.; et al. Global Threats to Human Water Security and River Biodiversity. *Nature* **2010**, *467*, 555–561. [[CrossRef](#)] [[PubMed](#)]
6. Tong, W.; Forster, M.; Dionigi, F.; Dresch, S.; Sadeghi Erami, R.; Strasser, P.; Cowan, A.J.; Farràs, P. Electrolysis of Low-Grade and Saline Surface Water. *Nat. Energy* **2020**, *5*, 367–377. [[CrossRef](#)]
7. Liu, X.; Chi, J.; Mao, H.; Wang, L. Principles of Designing Electrocatalyst to Boost Reactivity for Seawater Splitting. *Adv. Energy Mater.* **2023**, *13*, 2301438. [[CrossRef](#)]
8. Dionigi, F.; Reier, T.; Pawolek, Z.; Glied, M.; Strasser, P. Design Criteria, Operating Conditions, and Nickel-Iron Hydroxide Catalyst Materials for Selective Seawater Electrolysis. *ChemSusChem* **2016**, *9*, 962–972. [[CrossRef](#)]
9. Guo, J.; Zheng, Y.; Hu, Z.; Zheng, C.; Mao, J.; Du, K.; Jaroniec, M.; Qiao, S.-Z.; Ling, T. Direct Seawater Electrolysis by Adjusting the Local Reaction Environment of a Catalyst. *Nat. Energy* **2023**, *8*, 264–272. [[CrossRef](#)]
10. Bigiani, L.; Barreca, D.; Gasparotto, A.; Andreu, T.; Verbeeck, J.; Sada, C.; Modin, E.; Lebedev, O.I.; Morante, J.R.; Maccato, C. Selective Anodes for Seawater Splitting Via Functionalization of Manganese Oxides by a Plasma-Assisted Process. *Appl. Catal. B Environ.* **2021**, *284*, 119684. [[CrossRef](#)]
11. Xie, H.; Zhao, Z.; Liu, T.; Wu, Y.; Lan, C.; Jiang, W.; Zhu, L.; Wang, Y.; Yang, D.; Shao, Z. A Membrane-Based Seawater Electrolyser for Hydrogen Generation. *Nature* **2022**, *612*, 673–678. [[CrossRef](#)]
12. Kanan, M.W.; Nocera, D.G. In Situ Formation of an Oxygen-Evolving Catalyst in Neutral Water Containing Phosphate and Co<sup>2+</sup>. *Science* **2008**, *321*, 1072–1075. [[CrossRef](#)] [[PubMed](#)]
13. Costentin, C.; Nocera, D.G. Self-Healing Catalysis in Water. *Proc. Natl. Acad. Sci. USA* **2017**, *114*, 13380–13384. [[CrossRef](#)]
14. Thorarindottir, A.E.; Veroneau, S.S.; Nocera, D.G. Self-Healing Oxygen Evolution Catalysts. *Nat. Commun.* **2022**, *13*, 1243. [[CrossRef](#)] [[PubMed](#)]
15. Feng, C.; Wang, F.; Liu, Z.; Nakabayashi, M.; Xiao, Y.; Zeng, Q.; Fu, J.; Wu, Q.; Cui, C.; Han, Y.; et al. A Self-Healing Catalyst for Electrocatalytic and Photoelectrochemical Oxygen Evolution in Highly Alkaline Conditions. *Nat. Commun.* **2021**, *12*, 5980. [[CrossRef](#)] [[PubMed](#)]

16. Chung, D.Y.; Lopes, P.P.; Farinazzo Bergamo Dias Martins, P.; He, H.; Kawaguchi, T.; Zapol, P.; You, H.; Tripkovic, D.; Strmcnik, D.; Zhu, Y.; et al. Dynamic Stability of Active Sites in Hydr(Oxy)Oxides for the Oxygen Evolution Reaction. *Nat. Energy* **2020**, *5*, 222–230. [[CrossRef](#)]
17. Hou, Y.; Wang, F.; Qin, C.; Wu, S.; Cao, M.; Yang, P.; Huang, L.; Wu, Y. A Self-Healing Electrocatalytic System Via Electrohydrodynamics Induced Evolution in Liquid Metal. *Nat. Commun.* **2022**, *13*, 7625. [[CrossRef](#)] [[PubMed](#)]
18. Fang, S.; Tu, W.; Mu, L.; Sun, Z.; Hu, Q.; Yang, Y. Saline Alkali Water Desalination Project in Southern Xinjiang of China: A Review of Desalination Planning, Desalination Schemes and Economic Analysis. *Renew. Sustain. Energy Rev.* **2019**, *113*, 109268. [[CrossRef](#)]
19. Thangavel, P.; Ha, M.; Kumaraguru, S.; Meena, A.; Singh, A.N.; Harzandi, A.M.; Kim, K.S. Graphene-Nanoplatelets-Supported NiFe-MOF: High-Efficiency and Ultra-Stable Oxygen Electrodes for Sustained Alkaline Anion Exchange Membrane Water Electrolysis. *Energy Environ. Sci.* **2020**, *13*, 3447–3458. [[CrossRef](#)]
20. Wang, Y.; Yan, L.; Dastafkan, K.; Zhao, C.; Zhao, X.; Xue, Y.; Huo, J.; Li, S.; Zhai, Q. Lattice Matching Growth of Conductive Hierarchical Porous MOF/LDH Heteronanotube Arrays for Highly Efficient Water Oxidation. *Adv. Mater.* **2021**, *33*, e2006351. [[CrossRef](#)]
21. Sun, Y.; Ding, S.; Xu, S.; Duan, J.; Chen, S. Metallic Two-Dimensional Metal-Organic Framework Arrays for Ultrafast Water Splitting. *J. Power Sources* **2021**, *494*, 229733. [[CrossRef](#)]
22. Sun, Y.; Xu, S.; Ortiz-Ledon, C.A.; Zhu, J.; Chen, S.; Duan, J. Biomimetic Assembly to Superplastic Metal-Organic Framework Aerogels for Hydrogen Evolution from Seawater Electrolysis. *Exploration* **2021**, *1*, 20210021. [[CrossRef](#)] [[PubMed](#)]
23. Li, J.; Huang, W.; Wang, M.; Xi, S.; Meng, J.; Zhao, K.; Jin, J.; Xu, W.; Wang, Z.; Liu, X.; et al. Low-Crystalline Bimetallic Metal-Organic Framework Electrocatalysts with Rich Active Sites for Oxygen Evolution. *ACS Energy Lett.* **2018**, *4*, 285–292. [[CrossRef](#)]
24. Sun, F.; Wang, G.; Ding, Y.; Wang, C.; Yuan, B.; Lin, Y. NiFe-Based Metal-Organic Framework Nanosheets Directly Supported on Nickel Foam Acting as Robust Electrodes for Electrochemical Oxygen Evolution Reaction. *Adv. Energy Mater.* **2018**, *8*, 1800584. [[CrossRef](#)]
25. Marques, L.F.; Santos, H.P.; Correa, C.C.; Resende, J.A.L.C.; da Silva, R.R.; Ribeiro, S.J.L.; Machado, F.C. Construction of a Series of Rare Earth Metal-Organic Frameworks Supported by Thiophenedicarboxylate Linker: Synthesis, Characterization, Crystal Structures and near-Infrared/Visible Luminescence. *Inorg. Chim. Acta* **2016**, *451*, 41–51. [[CrossRef](#)]
26. Wang, G.X.; Shang, L.L.; Li, Z.H.; Zhao, B.T. A New Two-Dimensional Manganese(II) Coordination Polymer Based on Thiophene-3,4-Dicarboxylic Acid. *Acta Crystallogr. C* **2014**, *70*, 715–717. [[CrossRef](#)]
27. Fei, H.; Liu, X.; Li, Z.; Feng, W. Synthesis of Manganese Coordination Polymer Microspheres for Lithium-Ion Batteries with Good Cycling Performance. *Electrochim. Acta* **2015**, *174*, 1088–1095. [[CrossRef](#)]
28. Luo, R.; Li, Y.; Xing, L.; Wang, N.; Zhong, R.; Qian, Z.; Du, C.; Yin, G.; Wang, Y.; Du, L. A Dynamic Ni(OH)<sub>2</sub>-NiOOH/NiFeP Heterojunction Enabling High-Performance E-Upgrading of Hydroxymethylfurfural. *Appl. Catal. B Environ.* **2022**, *311*, 121357. [[CrossRef](#)]
29. Wu, B.; Gong, S.; Lin, Y.; Li, T.; Chen, A.; Zhao, M.; Zhang, Q.; Chen, L. A Unique NiOOH@FeOOH Heteroarchitecture for Enhanced Oxygen Evolution in Saline Water. *Adv. Mater.* **2022**, *34*, e2108619. [[CrossRef](#)]
30. Wu, Y.; Zhao, Y.; Zhai, P.; Wang, C.; Gao, J.; Sun, L.; Hou, J. Triggering Lattice Oxygen Activation of Single-Atomic Mo Sites Anchored on Ni-Fe Oxyhydroxides Nanoarrays for Electrochemical Water Oxidation. *Adv. Mater.* **2022**, *34*, e2202523. [[CrossRef](#)]
31. Hu, Q.; Wang, Z.; Huang, X.; Qin, Y.; Yang, H.; Ren, X.; Zhang, Q.; Liu, J.; Shao, M.; He, C. Integrating Well-Controlled Core-Shell Structures into “Superaerophobic” Electrodes for Water Oxidation at Large Current Densities. *Appl. Catal. B Environ.* **2021**, *286*, 119920. [[CrossRef](#)]
32. Huang, L.F.; Hutchison, M.J.; Santucci, R.J.; Scully, J.R.; Rondinelli, J.M. Improved Electrochemical Phase Diagrams from Theory and Experiment: The Ni-Water System and Its Complex Compounds. *J. Phys. Chem. C* **2017**, *121*, 9782–9789. [[CrossRef](#)]
33. Wang, H.; Li, M.; Duan, J.; Chen, S. Porous yet Densely Packed Metal-Organic Frameworks (MOFs) toward Ultrastable Oxygen Evolution at Practical Current Densities. *Mater. Chem. Front.* **2023**, *7*, 5005–5014. [[CrossRef](#)]
34. Trotochaud, L.; Young, S.L.; Ranney, J.K.; Boettcher, S.W. Nickel-Iron Oxyhydroxide Oxygen-Evolution Electrocatalysts: The Role of Intentional and Incidental Iron Incorporation. *J. Am. Chem. Soc.* **2014**, *136*, 6744–6753. [[CrossRef](#)]
35. Yang, F.; Lopez Luna, M.; Haase, F.T.; Escalera-Lopez, D.; Yoon, A.; Ruscher, M.; Rettenmaier, C.; Jeon, H.S.; Ortega, E.; Timoshenko, J.; et al. Spatially and Chemically Resolved Visualization of Fe Incorporation into NiO Octahedra During the Oxygen Evolution Reaction. *J. Am. Chem. Soc.* **2023**, *145*, 21465–21474. [[CrossRef](#)] [[PubMed](#)]
36. Liu, J.; Du, W.; Guo, S.; Pan, J.; Hu, J.; Xu, X. Iron-Locked Hydr(Oxy)Oxide Catalysts Via Ion-Compensatory Reconstruction Boost Large-Current-Density Water Oxidation. *Adv. Sci.* **2023**, *10*, e2300717. [[CrossRef](#)] [[PubMed](#)]
37. Liang, L.; Zhu, Q.; Shi, L.; Wang, F.; Ma, J.; Sun, J. The Efficient Removal of Dyes over Magnetic Ni Embedded on Mesoporous Graphitic Carbon Material. *J. Porous Mater.* **2014**, *21*, 985–991. [[CrossRef](#)]
38. Wan, Z.; Yang, D.; Chen, J.; Tian, J.; Isimjan, T.T.; Yang, X. Oxygen-Evolution Catalysts Based on Iron-Mediated Nickel Metal-Organic Frameworks. *ACS Appl. Nano Mater.* **2019**, *2*, 6334–6342. [[CrossRef](#)]
39. Hu, S.; Li, Y.; Kim, D.; Liu, M.; Lee, L.Y.S.; Wong, K.Y. Surface Modulated Fe Doping of  $\beta$ -Ni(OH)<sub>2</sub> Nanosheets for Highly Promoted Oxygen Evolution Electrocatalysis. *EcoMat* **2022**, *4*, e12256. [[CrossRef](#)]

40. Tian, J.; Jiang, F.; Yuan, D.; Zhang, L.; Chen, Q.; Hong, M. Electric-Field Assisted in Situ Hydrolysis of Bulk Metal-Organic Frameworks (MOFs) into Ultrathin Metal Oxyhydroxide Nanosheets for Efficient Oxygen Evolution. *Angew. Chem. Int. Ed.* **2020**, *59*, 13101–13108. [[CrossRef](#)]
41. Wu, X.; Song, X.; Tan, H.; Kang, Y.; Zhao, Z.; Jin, S.; Chang, X. Deciphering the Structure Evolution and Active Origin for Electrochemical Oxygen Evolution over Ni<sub>3</sub>S<sub>2</sub>. *Mater. Today Energy* **2022**, *26*, 101008. [[CrossRef](#)]
42. Li, X.; Zhou, J.; Liu, C.; Xu, L.; Lu, C.; Yang, J.; Pang, H.; Hou, W. Encapsulation of Janus-Structured Ni/Ni<sub>2</sub>P Nanoparticles within Hierarchical Wrinkled N-Doped Carbon Nanofibers: Interface Engineering Induces High-Efficiency Water Oxidation. *Appl. Catal. B Environ.* **2021**, *298*, 120578. [[CrossRef](#)]
43. Bai, Y.; Wu, Y.; Zhou, X.; Ye, Y.; Nie, K.; Wang, J.; Xie, M.; Zhang, Z.; Liu, Z.; Cheng, T.; et al. Promoting Nickel Oxidation State Transitions in Single-Layer NiFeB Hydroxide Nanosheets for Efficient Oxygen Evolution. *Nat. Commun.* **2022**, *13*, 6094. [[CrossRef](#)]
44. Park, J.; Kim, J.; Lee, S.; Kim, J.H.; Yoon, M.-H.; Lee, D.; Yoo, S.J. Unraveling Concentration-Dependent Solvation Structures and Molecular Interactions in Water-in-Salt Electrolytes for Enhanced Performance of Electric Double-Layer Capacitors. *Energy Storage Mater.* **2024**, *65*, 103137. [[CrossRef](#)]
45. Chen, S.; Wang, T.; Ma, L.; Zhou, B.; Wu, J.; Zhu, D.; Li, Y.Y.; Fan, J.; Zhi, C. Aqueous Rechargeable Zinc Air Batteries Operated at –110 °C. *Chem* **2023**, *9*, 497–510. [[CrossRef](#)]
46. Stevens, M.B.; Enman, L.J.; Batchellor, A.S.; Cosby, M.R.; Vise, A.E.; Trang, C.D.M.; Boettcher, S.W. Measurement Techniques for the Study of Thin Film Heterogeneous Water Oxidation Electrocatalysts. *Chem. Mater.* **2016**, *29*, 120–140. [[CrossRef](#)]
47. Gorlin, M.; Chernev, P.; Ferreira de Araujo, J.; Reier, T.; Drespe, S.; Paul, B.; Krahnert, R.; Dau, H.; Strasser, P. Oxygen Evolution Reaction Dynamics, Faradaic Charge Efficiency, and the Active Metal Redox States of Ni-Fe Oxide Water Splitting Electrocatalysts. *J. Am. Chem. Soc.* **2016**, *138*, 5603–5614. [[CrossRef](#)]
48. Costa, P.; Sandrin, D.; Scaiano, J.C. Real-Time Fluorescence Imaging of a Heterogeneously Catalysed Suzuki-Miyaura Reaction. *Nat. Catal.* **2020**, *3*, 427–437. [[CrossRef](#)]
49. Do, V.-H.; Prabhu, P.; Li, Y.; Xie, W.; Kidkhunthod, P.; Wang, G.; Wang, X.; Lee, J.-M. Surface Activation of Atomically Thin Metal Nitride by Confined Nanoclusters to Trigger pH-Universal Hydrogen Evolution. *Joule* **2023**, *7*, 2118–2134. [[CrossRef](#)]
50. Li, Y.; Bo, T.; Zuo, S.; Zhang, G.; Zhao, X.; Zhou, W.; Wu, X.; Zhao, G.; Huang, H.; Zheng, L.; et al. Reversely Trapping Isolated Atoms in High Oxidation State for Accelerating the Oxygen Evolution Reaction Kinetics. *Angew. Chem. Int. Ed.* **2023**, *62*, e202309341. [[CrossRef](#)]
51. Tariq, I.; Asghar, M.A.; Ali, A.; Badshah, A.; Abbas, S.M.; Iqbal, W.; Zubair, M.; Haider, A.; Zaman, S. Surface Reconstruction of Cobalt-Based Polyoxometalate and CNT Fiber Composite for Efficient Oxygen Evolution Reaction. *Catalysts* **2022**, *12*, 1242. [[CrossRef](#)]
52. Zhong, H.; Zhang, Q.; Yu, J.; Zhang, X.; Wu, C.; Ma, Y.; An, H.; Wang, H.; Zhang, J.; Wang, X.; et al. Fundamental Understanding of Structural Reconstruction Behaviors in Oxygen Evolution Reaction Electrocatalysts. *Adv. Energy Mater.* **2023**, *13*, 2301391. [[CrossRef](#)]
53. Cao, J.; Mou, T.; Mei, B.; Yao, P.; Han, C.; Gong, X.; Song, P.; Jiang, Z.; Frauenheim, T.; Xiao, J.; et al. Improved Electrocatalytic Activity and Stability by Single Iridium Atoms on Iron-Based Layered Double Hydroxides for Oxygen Evolution. *Angew. Chem. Int. Ed.* **2023**, *62*, e202310973. [[CrossRef](#)] [[PubMed](#)]
54. Li, N.; Bediako, D.K.; Hadt, R.G.; Hayes, D.; Kempa, T.J.; von Cube, F.; Bell, D.C.; Chen, L.X.; Nocera, D.G. Influence of Iron Doping on Tetravalent Nickel Content in Catalytic Oxygen Evolving Films. *Proc. Natl. Acad. Sci. USA* **2017**, *114*, 1486–1491. [[CrossRef](#)] [[PubMed](#)]
55. Yu, L.; Wu, L.; McElhenny, B.; Song, S.; Luo, D.; Zhang, F.; Yu, Y.; Chen, S.; Ren, Z. Ultrafast Room-Temperature Synthesis of Porous S-Doped Ni/Fe (Oxy)Hydroxide Electrodes for Oxygen Evolution Catalysis in Seawater Splitting. *Energy Environ. Sci.* **2020**, *13*, 3439–3446. [[CrossRef](#)]
56. McCrory, C.C.; Jung, S.; Peters, J.C.; Jaramillo, T.F. Benchmarking Heterogeneous Electrocatalysts for the Oxygen Evolution reaction. *J. Am. Chem. Soc.* **2013**, *135*, 16977–16987. [[CrossRef](#)]
57. Zheng, W.; Liu, M.; Lee, L.Y.S. Best Practices in Using Foam-Type Electrodes for Electrocatalytic Performance Benchmark. *ACS Energy Lett.* **2020**, *5*, 3260–3264. [[CrossRef](#)]
58. Zhang, L.; Liang, J.; Yue, L.; Dong, K.; Li, J.; Zhao, D.; Li, Z.; Sun, S.; Luo, Y.; Liu, Q.; et al. Benzoate Anions-Intercalated NiFe-layered Double Hydroxide Nanosheet Array with Enhanced Stability for Electrochemical Seawater Oxidation. *Nano Res. Energy* **2022**, *1*, e9120028. [[CrossRef](#)]
59. Wu, L.; Yu, L.; Zhu, Q.; McElhenny, B.; Zhang, F.; Wu, C.; Xing, X.; Bao, J.; Chen, S.; Ren, Z. Boron-modified Cobalt Iron Layered Double Hydroxides for High Efficiency Seawater Oxidation. *Nano Energy* **2021**, *83*, 105838. [[CrossRef](#)]
60. Wu, L.; Yu, L.; McElhenny, B.; Xing, X.; Luo, D.; Zhang, F.; Bao, J.; Chen, S.; Ren, Z. Rational Design of Core-shell-structured CoP@FeOOH for Efficient Seawater Electrolysis. *Appl. Catal. B Environ.* **2021**, *294*, 120256. [[CrossRef](#)]
61. Zhang, L.; Wang, Z.; Qiu, J. Energy-Saving Hydrogen Production by Seawater Electrolysis Coupling Sulfion Degradation. *Adv. Mater.* **2022**, *34*, e2109321. [[CrossRef](#)] [[PubMed](#)]
62. Huang, C.; Zhou, Q.; Yu, L.; Duan, D.; Cao, T.; Qiu, S.; Wang, Z.; Guo, J.; Xie, Y.; Li, L.; et al. Functional Bimetal Co-Modification for Boosting Large-Current-Density Seawater Electrolysis by Inhibiting Adsorption of Chloride Ions. *Adv. Energy Mater.* **2023**, *13*, 2301475. [[CrossRef](#)]

63. Wu, L.; Yu, L.; Zhang, F.; McElhenny, B.; Luo, D.; Karim, A.; Chen, S.; Ren, Z. Heterogeneous Bimetallic Phosphide Ni<sub>2</sub>P-Fe<sub>2</sub>P as an Efficient Bifunctional Catalyst for Water/Seawater Splitting. *Adv. Funct. Mater.* **2020**, *31*, 2006484. [[CrossRef](#)]
64. Wang, C.; Zhu, M.; Cao, Z.; Zhu, P.; Cao, Y.; Xu, X.; Xu, C.; Yin, Z. Heterogeneous Bimetallic Sulfides Based Seawater Electrolysis towards Stable Industrial-level Large Current Density. *Appl. Catal. B Environ.* **2021**, *291*, 120071. [[CrossRef](#)]
65. Lan, C.; Xie, H.; Wu, Y.; Chen, B.; Liu, T. Nanoengineered, Mo-Doped, Ni<sub>3</sub>S<sub>2</sub> Electrocatalyst with Increased Ni-S Coordination for Oxygen Evolution in Alkaline Seawater. *Energy Fuels* **2022**, *36*, 2910–2917. [[CrossRef](#)]
66. Yu, L.; Zhu, Q.; Song, S.; McElhenny, B.; Wang, D.; Wu, C.; Qin, Z.; Bao, J.; Yu, Y.; Chen, S.; et al. Non-noble Metal-nitride Based Electrocatalysts for High-performance Alkaline Seawater Electrolysis. *Nat. Commun.* **2019**, *10*, 5106. [[CrossRef](#)]
67. Kuang, Y.; Kenney, M.J.; Meng, Y.; Hung, W.H.; Liu, Y.; Huang, J.E.; Prasanna, R.; Li, P.; Li, Y.; Wang, L.; et al. Solar-driven, Highly Sustained Splitting of Seawater into Hydrogen and Oxygen Fuels. *Proc. Natl. Acad. Sci. USA* **2019**, *116*, 6624–6629. [[CrossRef](#)]
68. Chen, H.; Zou, Y.; Li, J.; Zhang, K.; Xia, Y.; Hui, B.; Yang, D. Wood Aerogel-derived Sandwich-like Layered Nanoelectrodes for Alkaline Overall Seawater Electrosplitting. *Appl. Catal. B Environ.* **2021**, *293*, 120215. [[CrossRef](#)]

**Disclaimer/Publisher’s Note:** The statements, opinions and data contained in all publications are solely those of the individual author(s) and contributor(s) and not of MDPI and/or the editor(s). MDPI and/or the editor(s) disclaim responsibility for any injury to people or property resulting from any ideas, methods, instructions or products referred to in the content.